Evaluation of numerical strategies for Large Eddy Simulation of particulate two-phase recirculating flows

Riber E. [a,b,*], Moureau V. [c], García M. [b], Poinsot T. [a] and Simonin O. [a]

[a] *IMFT-UMR 5502, allée du Professeur Camille Soula. 31400 Toulouse. France*

[b] *CERFACS, 42, avenue Gaspard Coriolis. 31057 Toulouse Cedex 01. France*

[c] *CTR, Stanford University, Stanford, CA 94305-3030, USA*

Abstract

Predicting particle dispersion in recirculating two-phase flows is a key issue for reacting flows and a potential application of Large Eddy Simulation (LES) methods. In this study, Euler/Euler and Euler/Lagrange LES approaches are compared in the bluff body configuration from Borée *et al.* [1] where glass beads are injected into a complex recirculating flow. These tests are performed for non-reacting, non-evaporating sprays but are mandatory validations before computing realistic combustion chambers. Two different codes (one explicit and compressible and the other implicit and incompressible) are also tested on the same configuration. Results show that the gas flow is well predicted by both codes. The dispersed phase is also well predicted by both codes but the Lagrangian approach predicts root-mean-square values more accurately than the Eulerian approach. The effects of mesh, solvers and numerical schemes are discussed for each method.

Key words: LES, two-phase recirculating flows, particles, Euler/Lagrange, Euler/Euler.

1 Introduction

Today, RANS (Reynolds-averaged Navier-Stokes) equations are routinely solved to design combustion chambers, for both gaseous and liquid fuels. Recently, Large Eddy Simulation (LES) has been extended to reacting gaseous flows in order to give access to unsteady phenomena occurring in combustion devices (such as instabilities, flashback or quenching), and to provide better accuracy for the prediction of mean flows. The success of these approaches for gaseous flames in the last years [2,3,4,5,6,7,8,9,10,11,12] is a clear illustration of their potential. LES gives access to the large scales structures of the flow, reducing the importance of modeling, and capturing a significant part of the physics controlling these flames.

Even though LES has already demonstrated its potential for gaseous flames, its extension to two-phase flames is still largely to be done. First, the physical submodels required to describe the atomization of a liquid fuel jet, the dispersion of fuel droplets, their interaction with walls, evaporation and combustion are as difficult to build in LES as in RANS because they are essentially subgrid phenomena. Second, the numerical implementation of two-phase flow LES remains a challenge: the equations for both the gaseous and the dispersed phases must be solved together at each time step in a strongly coupled manner. This differs from classical RANS where the resolution of the two phases can be done in a weak procedure, bringing first the gas flow to convergence, then the solid particles and iterating until convergence of both phases. Finally, in the context of parallel supercomputing, numerical efficiency is an additional constraint. For single-phase flows, efficient and accurate solvers have been developed and speedups of the order of 5000 are not uncommon [13]. Representing the main physics of two-phase flows while maintaining a similar parallel efficiency for

* Corresponding author.
Email address: ele.riber@gmail.com (Riber E.).

two-phase flow solvers raises additional questions: particle/mesh load imbalance is a crucial issue in Euler/Lagrange simulations, as discussed for instance in [14,15].

In LES of reacting two-phase flows, physics and numerics interact strongly: the first question is to choose a paradigm to describe the two-phase flow. In dilute particle-laden flows, most RANS codes use Euler/Lagrange (EL) methods in which the gas flow is solved using an Eulerian method and the particles are tracked using a Lagrangian approach. An alternative technique is to use Euler/Euler (EE) methods in which both phases are solved using an Eulerian approach. The history of RANS development has shown that the EL and EE methods both show advantages and disadvantages depending on the application. Consequently, both approaches are found today in most commercial codes. For LES, both EE and EL approaches are being developed and the focus of this study is to test and compare them in a reference case where complete sets of experimental results for gas and dispersed phase are available. This exercise is performed here without evaporation or combustion: the droplets are replaced by solid particles.

2 Flow configuration and work objectives

2.1 Choice of the configuration

In combustion chambers, the flame resulting from a free jet flow would be too long compared to the dimensions of the chamber, and also very difficult to stabilize. Therefore, most combustion devices are designed so as to anchor the flame at a specific location. The use of a flame holder is often difficult due to the very high temperatures that may damage the device itself. Another possibility is to stabilize the flame behind a sudden expansion like a backward-facing step:

the flow is strongly decelerated forming a corner recirculation zone, and the recirculating hot gases then provoke the ignition of the incoming fresh gases. As far as aeronautical combustion chambers are concerned, highly swirling flows that pass through a sudden expansion are preferred since they provide a more compact stabilized flame. A central toroidal recirculation zone is created, acting as a flame holder in the center of the flow, close to the injector tip. In such devices, the recirculation zones induce high turbulence levels and high mixing rates, stabilizing the flame and reducing pollutant emissions.

Before computing reactive two-phase flows in such devices, a validation of the turbulent dispersion of the particles in similar flows is needed. Indeed, the accurate description of the fuel droplet motion is crucial to determine first the resulting fuel vapor distribution, and then the combustion mode and the pollutant emissions among others. With aeronautical applications in prospect, the bluff body flow from Borée *et al.* [1] is a very interesting configuration. First, it exhibits the same flow structures as combustion chambers, with corner recirculation zones and stagnation points. To predict their location, a precise description of the large structures and the intermittency of the fluid flow is required [16,17,18]. Second, the particle motion is complex: depending on their inertia, the fuel droplets are captured in the recirculation zones or cross them. Since they are then vaporised, they directly determine the gaseous fuel field, and consequently the burner efficiency as well as the pollutant emissions [19,20]. Then, as very few particles reach the external walls of the chamber, the particle-wall interactions can be neglected in this configuration, which simplifies the comparison between both methods. Indeed, modeling particle motion in wall-bounded flows is still a challenge despite multiple studies using either the EL approach [21,22,23,24] or the EE approach [25,26,27]. Furthermore, in a hot combustion chamber where liquid fuel is injected, the fuel droplets often evaporate rapidly and the interaction between particles and solid walls is not a crucial mechanism. If not, a liquid film develops on the walls, which requires

specific modeling [28]. Finally, a large amount of data is provided by Borée *et al.* [1], including mean and fluctuating quantities for both phases, which allows to validate not only the gas LES models, but also the dispersed phase modeling.

2.2 Description of the experimental setup

The configuration of Borée *et al.* [1] consists of a vertical axisymmetrical particle-laden confined bluff body flow (see Fig. 1) on the flow loop Hercule of EDF-R&D [1] . Air blowers are used to generate the coflow whereas both air and glass beads are injected in the inner pipe. The measurement zone is located at $z = 0$ downstream of the inner and annular ducts, where large recirculation zones are created between the central jet and the coflow. Thus, the resulting flow is very similar to the ones obtained in industrial combustion devices, where fuel droplets are injected together with air. Hereafter, the symbols $\cdot_f$ and $\cdot_p$ denote the fluid and the particles.

2.2.1 The gas phase

Schefer *et al.* [17] show that the topology of a turbulent bluff body flow strongly depends on the ratio $\bar{U}_{f,I}/\bar{U}_{f,C}$, where $\bar{U}$ is a bulk velocity and the subscripts I and C denote the inner pipe and the coflow respectively. Depending on the velocity ratio $\bar{U}_{f,I}/\bar{U}_{f,C}$, there are three possible flow topologies [17]. In Fig. 2, sketches of mean gas velocity vectors are drawn for three decreasing velocity ratios ($\bar{U}_{f,I}/\bar{U}_{f,C} = 2.8$, 1.4 and 0.84) whereas in Fig. 3, the gas flow is seeded with small particles to give access to the flow topology for the same three velocity ratios:

[1] Électricité de France - Recherche & Développement

(1) For the highest velocity ratio ($\bar{U}_{f,I}/\bar{U}_{f,C} = 2.8$), the flow along the axis is similar to a free jet flow. The air flows coming from the inner and annular pipes converge far from the outlet of the inner duct. Two counter-rotative eddies separate the two flows before they converge. There are two stagnation points on both sides of the central jet.

(2) At lower velocity ratio ($\bar{U}_{f,I}/\bar{U}_{f,C} = 1.4$), a single stagnation point is formed along the centerline and the flow looks like a non-penetrating jet.

(3) Finally, for the smallest velocity ratio ($\bar{U}_{f,I}/\bar{U}_{f,C} = 0.84$), a second stagnation point appears on the axis whose location is linked to the geometry global parameter. The second stagnation point remains close to the chamber inlet and does not move any longer when the ratio $\bar{U}_{f,I}/\bar{U}_{f,C}$ becomes lower.

The experiments of Borée *et al.* [1] are conducted at ambient temperature and standard pressure: $T_f = 293\ K$ and $P_f = 10^5\ Pa$. The radius of the inner pipe is $R_I = 10\ mm$. The air volume flux of the inner pipe is $Q_{f,I} = 3.4\ m^3.h^{-1}$, which corresponds to a mean velocity $\bar{U}_{f,I} = 3.4\ m.s^{-1}$, whereas the maximum velocity in the inner duct reaches $U_{f,I}^{max} = 4\ m.s^{-1}$. Although the Reynolds number is rather moderate ($Re_I = 2R_I\bar{U}_{f,I}/\nu_f \approx 4500$, where ν_f is the kinematic viscosity of the fluid), the ratio $U_{f,I}^{max}/\bar{U}_{f,I} = 1.18$ at the outlet of the inner pipe is however consistent with developed turbulent pipe flow.
The dimensions of the annular outer region are: $R_{C,1} = 75\ mm$, $R_{C,2} = 150\ mm$. The air volume flux in the coflow is $Q_{f,C} = 780\ m^3.h^{-1}$, which corresponds to mean and maximum velocities equal to: $\bar{U}_{f,C} = 4.1\ m.s^{-1}$ and $U_{f,C}^{max} = 6\ m.s^{-1}$. The associated Reynolds number of the annular jet is $Re_C = 2\,(R_{C,2} - R_{C,1})\,\bar{U}_{f,C}/\nu_f \approx 40{,}000$. The main characteristics of the configuration are summarised in Table 1.

The velocity ratio $\bar{U}_{f,I}/\bar{U}_{f,C}$ considered by Borée *et al.* [1] is 0.83. Following Schefer *et al.* [17], there are two stagnation points along the centerline.

Choosing a ratio lower than one creates a complex gas flow behaviour when modeling particle dispersion: depending on their inertia, the particles remain in the recirculation zone delimited by the two stagnation points or leave it.

2.2.2 The dispersed phase

In Borée *et al.* [1], polydisperse glass particles with material density $\rho_p = 2470\ kg.m^{-3}$, are injected in the inner pipe only through a particle feeder. Two mass fluxes of glass beads, $Q^1_{p,I} = 1\ kg.h^{-1}$ and $Q^2_{p,I} = 5\ kg.h^{-1}$, have been used experimentally to study the influence of particle inertia on the two-phase flow as well as the role of inter-particle interactions. The corresponding mass loading in the inner duct then varies from $M^1_{p,I} = 22\ \%$ to $M^2_{p,I} = 110\ \%$. In this study, only the lowest mass loading case is considered.
Particle diameter covers a wide range of size classes from $d_p = 20\ \mu m$ to $d_p = 100\ \mu m$. Figure 4 shows the initial particle distribution, in mass (M) and in number (N). The resulting mean diameters are respectively $d_{p,M} = 63\ \mu m$ and $d_{p,N} = 50\ \mu m$. Characterising the particle distribution using a Particle Doppler Anemometry (PDA) method [29] requires special care: the glass beads should remain spherical and the inter-particle collision should not induce any particle break-up. Therefore, Borée *et al.* [1] repeated the measurements and used a microscope to verify the shape and size of particles.

2.2.3 Characteristic time scales of the two-phase flow

Table 2 gives the particle relaxation time τ_p depending on the particle diameter d_p. In a first approximation, Stokes flow around the particles is assumed so that τ_p reads:

$$\tau_p = \frac{\rho_p d_p^2}{18\mu_f}\ , \tag{1}$$

where μ_f is the dynamic viscosity of the fluid.
The comparison of the particle relaxation time with a characteristic time scale

of the fluid most energetic eddies $\tau_{f,t}$, yields the Stokes number St. To evaluate $\tau_{f,t}$ at the outlet of the inner pipe, the length of the most energetic eddies is estimated as a third of the pipe diameter and their velocity as the maximum fluctuating velocity in the pipe:

$$St = \frac{\tau_p}{\tau_{f,t}} \qquad \text{where} \qquad \tau_{f,t} = \frac{\frac{2R_I}{3}}{u'^{max}_{f,I}} \approx 7\ ms\ . \tag{2}$$

Table 2 presents the characteristic Stokes number of the particles depending on their diameter: the smallest particles with diameter $d_p = 20\ \mu m$ almost follow the gas flow while the inertia of the biggest ones with diameter $d_p = 100\ \mu m$ makes them much more independent of the fluid flow.

As underlined by Schefer *et al.* [30], the recirculation zones and the stagnation points are related to the inner and outer pipe flow characteristics. However in the inner pipe (whose diameter is small), the motion of the particles is complex, due to interactions with the fluid and the walls as well as inter-particle collisions. To quantify whether particles have time to adapt to changes in gas mean velocity within the inner duct, the particle relaxation time is compared to their transit time T_p^T in the pipe:

$$T_p^T = \frac{L_I}{U^{max}_{f,I}} = 500\ ms\ , \tag{3}$$

where $L_I = 2\ m$ is the length of the inner duct that particles travel accross and $U^{max}_{f,I}$ is the inner maximum gas velocity. Compared to the particle relaxation time, the particle transit time of all particles in the inner pipe remains large. Thus, the particles have time to adapt to fluid turbulence before they reach the outlet of the inner pipe.

2.3 Objectives of the simulations

In this study two unstructured codes developed at CERFACS and CTR are used to investigate the configuration of Borée *et al.* [1]:

(1) an explicit compressible code (AVBP) using both EL and mesoscopic EE [31,32,33] approaches. For the present study, AVBP is used on both hexahedron-based and tetrahedron-based grids;
(2) an implicit incompressible code (CDP) using a EL formulation. For this study, hexahedron-based grids are used in CDP.

The dispersed phase consists of solid particles so that evaporation, coalescence and break up do not have to be considered. Accounting for polydispersion in the bluff body configuration using EL approaches is straightforward: particles with different diameters are injected at the inlet of the chamber. When using EE approaches, there are two main methods. On the one hand, polydispersion can be accounted for by introducing a particle size distribution [34]. On the other hand, EE approaches can be extended to polydispersion using a multi-class method: the set of particulate equations is resolved for a finite number of particle classes depending on their diameter. The main disadvantage of this method is its computational cost which drastically increases with the number of classes to be considered. In the specific case of Borée *et al.* [1] experiments, separate studies (not reported here) using Lagrangian simulations and polydisperse particles or 60 μm particles only have shown that using a monodisperse distribution of size was very close to the 22 % case of Borée *et al.* [1] and was sufficient to capture both the mean flow effects on the gas (through two-way coupling) and the dynamics of the 60 μm class. Therefore in this work, particle distribution is assumed monodisperse with particle diameter close to the initial mean diameter in mass: $d_p = 60\ \mu m$. Only the low mass loading case ($M_p = 22$ %) of Borée *et al.* [1] is studied. Since the particle volume fraction α_p is about 1 % at the inlet, interparticle collisions are found to play a crucial role in the injection tube [35]. Nevertheless, the dilution effect being very effective, collision effect may be neglected in the modeling approaches for the numerical simulation of the downstream two-phase flow. Furthermore, the two-way coupling is taken into account through drag force. However, its

impact on the gas phase has been shown of minor importance in the 22 % mass loading case [1]. This case allows to study the following points:

(1) evaluate influence of mesh type (hexahedra vs tetrahedra);
(2) evaluate influence of numerical convective scheme (2^{nd} and 3^{rd} order);
(3) compare implicit and explicit formulations for time advancement;
(4) compare accuracy of EE and EL approaches.

3 Description of solvers and models

3.1 Gas flow solvers

Numerical methods used in both LES solvers for the gas phase have been extensively described in the literature ([9,7,36] for CDP and [8,12] for AVBP) and will only be summarized here.

The explicit LES solver AVBP solves the compressible Navier-Stokes equations with a second-order finite-volume Lax-Wendroff scheme or a third-order finite-element scheme TTGC [37,9]. The WALE model [38] that predicts the right scaling for the fluid turbulent viscosity when approaching a solid boundary (i.e., $\nu_{f,t} = 0$) is used to model the subgrid stress tensor.

The LES solver CDP solves implicitly the incompressible Navier-Stokes equations. The time integration of CDP is based on the fractional-step method [39] and the space integration relies on a second-order central scheme that conserves the kinetic energy [7,36]. The dynamic Smagorinsky model [40] is used to model the subgrid stress tensor.

The boundary conditions for each solver are detailed in Section 4.3.

3.2 Dispersed phase flow solvers

The particles are assumed to be rigid spheres with diameter comparable or smaller than the Kolmogorov length scale. If the particle density is much larger than the fluid density, the forces acting on particles reduce to drag and gravity [41,42].

3.2.1 Euler/Lagrange approach

In EL simulations, the influence of the particles on the gas-phase momentum and energy equations is taken into account by using the point-force approximation in the general framework of the particle-in-cell method (PIC) [43,44,45,46,47], with standard single-phase subgrid turbulence modeling approaches. According to Boivin *et al.* [48], such an assumption is valid for small mass loading ratio (typically, $\alpha_p \rho_p / \rho_f \leq 1$) with response time larger than the subgrid turbulence characteristic time scale. In particular, the coupling force exerted by each particle on the fluid is projected onto the grid nodes. The weights in the projection operation are inversely proportional to the distances between the particle and the nodes of the containing cell.

With these assumptions, the particle equations of motion can then be written for a single particle as:

$$\frac{dx_{p,i}}{dt} = u_{p,i} \ , \tag{4}$$

$$\frac{du_{p,i}}{dt} = -\frac{3}{4} \, \frac{\rho_f}{\rho_p} \, \frac{C_D}{d_p} \, |\mathbf{v}_r| \, \mathrm{v}_{r,i} + g_i = -\frac{u_{p,i} - \tilde{u}_{f,i}}{\tau_p} + g_i \ . \tag{5}$$

The local drag coefficient in Eq. (5) is C_D and may be expressed in terms of the particle Reynolds number Re_p following Schiller and Nauman [49]:

$$C_D = \frac{24}{Re_p} \left[1 + 0.15 Re_p^{0.687} \right], \qquad Re_p = \frac{|\mathbf{v}_r| \, d_p}{\nu_f} \leq 800 \ , \tag{6}$$

where τ_p is the particle relaxation time defined as:

$$\tau_p = \frac{4}{3} \, \frac{\rho_p}{\rho_f} \, \frac{d_p}{C_D \, |\mathbf{v}_r|} \ . \tag{7}$$

The local instantaneous relative velocity between the particle and the surrounding fluid is $v_{r,i} = u_{p,i} - \tilde{u}_{f,i}$, where $\tilde{u}_{f,i}$ is the fluid velocity at the position of the particle assuming that the flow field is locally undisturbed by the presence of this particle [42,50]. In first approximation, the velocity is assumed to be equal to the interpolation of the filtered velocity at the position of the particle [21,51,52]. The effect of the subgrid fluid turbulence is assumed to be negligible owing to the large inertia of the solid particles [53]. A linear interpolation algorithm is used to compute the fluid velocity at the position of the particle.

3.2.2 Euler/Euler approach

Eulerian equations for the dispersed phase may be derived by several means. A popular and simple way consists in volume filtering of the separate, local, instantaneous phase equations accounting for the inter-facial jump conditions [54]. Such an averaging approach is restrictive because the filter length must be both larger than the interparticle distance (to define continuous mean fields of particle number density and particle velocity), and smaller than the smallest length scale in the particle velocity field to ensure unicity of the particle velocity in the filtering volume. Moreover, Druzhinin [54] assumes that all the particles located in this filtering volume have the same velocity, which is untrue when the particle relaxation time is larger than the smallest turbulent time scale [32]. An alternative to the two-fluid approach is the Eulerian equilibrium approach proposed by Ferry and Balachandar [55] that reduces the number of transport equations to be solved: only the transport equation for particle number density is solved while the particle velocity is given by the expansion in τ_p of the local fluid quantities first proposed by Maxey [41] and then extended by Druzhinin [56], and Ferry and Balachandar [55]. Both approaches show good agreement with EL results when focusing on preferential concentration of low-inertia particles in HIT flows [41,57]. However, the er-

rors in the predictions of the particle field increase with the particle response time [58].

Though, the crucial assumption of the above approaches, the particle velocity uniqueness at a given position, fails when the particle relaxation time is larger than the Kolmogorov time scale, due to the crossing of particle trajectories. To overcome this difficulty, Février et al. [32], proposed a Probability Density Function (PDF) approach based on a conditional ensemble average of the particle properties for a given turbulent fluid flow realization. In such an approach, any discrete particle velocity may be separated into two contributions: an Eulerian velocity field, the mesoscopic velocity field shared by all the particle realizations, and a Lagrangian random distribution, the Random Uncorrelated Velocity (RUV), spatially uncorrelated and which accounts for the particle trajectory crossing. The conditional particle velocity PDF $\breve{f}_p(\mathbf{c}_p, \mathbf{x}, t)$ gives the local instantaneous probable number of particles with the given translation velocity $\mathbf{u}_p = \mathbf{c}_p$, and obeys a Boltzmann-type kinetic equation accounting for external forces acting on the particles and inter-particle collisions. The moments of the particle PDF are mesoscopic Eulerian quantities which obey transport equations derived by integration from the kinetic equation, following the same methodology than for the derivation of the Navier-Stokes equations in the frame of kinetic theory [59]. So, Février et al. [32] derived transport equations for particle number density $\bar{n}_p$, mesoscopic velocity $\breve{\mathbf{u}}_p$ and Random Uncorrelated kinetic Energy (RUE) $\delta\breve{\theta}_p$ and Simonin et al. [60] proposed, as a first approximation, a viscosity assumption to model the random uncorrelated kinetic stresses. The Mesoscopic approach was evaluated using *a priori* test from Discrete Particle Simulation (DPS) coupled with DNS or LES of forced homogeneous isotropic turbulence [61] and fully developed channel flow [22]. Then, by analogy with the gas phase, a LES filter is applied to the equations for the mesoscopic quantities [62,33], which leads to equations for the filtered (in the LES sense) particle number density $\bar{n}_p$ and the filtered correlated velocity $\hat{\mathbf{u}}_p$ using the mass-weighted averaging $\widehat{\bar{n}_p u_{p,j}} = \bar{n}_p \hat{u}_{p,j}$ [63]:

$$\frac{\partial}{\partial t}\bar{n}_p + \frac{\partial}{\partial x_j}\bar{n}_p\hat{u}_{p,j} = 0 \ , \tag{8}$$

$$\frac{\partial}{\partial t}\bar{n}_p\hat{u}_{p,i} + \frac{\partial}{\partial x_j}\bar{n}_p\hat{u}_{p,i}\hat{u}_{p,j} = -\frac{\bar{n}_p}{\tau_p}\left(\hat{u}_{p,i} - \hat{u}_{f,i}\right) + \bar{n}_p g_i - \frac{\partial}{\partial x_j}T_{p,ij} - \frac{\partial}{\partial x_j}\bar{n}_p\widehat{\delta R}^*_{p,ij} - \frac{\partial}{\partial x_i}\frac{2}{3}\bar{n}_p\widehat{\delta\theta}_p \ , \tag{9}$$

where $\bar{n}_p$, $\hat{\mathbf{u}}_p$, $\widehat{\delta R}^*_{p,ij}$ and $\widehat{\delta\theta}_p$ are respectively the filtered particle number density, the particle correlated velocity, the second-order uncorrelated particle velocity correlation tensor deviatoric, and the particle RUE. The first two terms of the Right-Hand-Side (RHS) of Eq. (9) are the drag force and gravity effects on large scales, the third one accounts for the subgrid-scale (SGS) effects, the fourth one is a diffusion term and the last one represents the pressure effect due to RUE. $T_{p,ij}$ stands for the particle subgrid stress tensor:

$$T_{p,ij} = \bar{n}_p(\widehat{u_{p,i}u_{p,j}} - \hat{u}_{p,i}\hat{u}_{p,j}) \ . \tag{10}$$

3.2.3 Filtered RUV and subgrid term modeling

Assuming small anisotropy of the RUM, Simonin *et al.* [64] model $\delta R^*_{p,ij}$ by a viscous term. For LES approaches this model is adapted by replacing non-filtered quantities by filtered ones leading to [62]:

$$\widehat{\delta R}^*_{p,ij} = -\hat{\nu}_{p,RUM}\left(\frac{\partial\hat{u}_{p,i}}{\partial x_j} + \frac{\partial\hat{u}_{p,j}}{\partial x_i} - \frac{2}{3}\frac{\partial\hat{u}_{p,k}}{\partial x_k}\delta_{ij}\right) \ , \tag{11}$$

where the RUM viscosity $\hat{\nu}_{p,RUM}$ is obtained in the framework of the kinetic theory of particulate flows [61]:

$$\hat{\nu}_{p,RUM} = \frac{\tau_p}{3}\widehat{\delta\theta}_p \ . \tag{12}$$

For the SGS tensor $T_{p,ij}$, Riber *et al.* [65] propose a viscosity model by analogy with single-phase flows [66,67]. The trace-free SGS tensor is modeled using a viscosity assumption (compressible Smagorinsky model), while the subgrid

energy is parametrized by a Yoshizawa model [68]:

$$T_{p,ij} = -C_S 2\Delta_f^2 \bar{n}_p |\hat{S}_p| (\hat{S}_{p,ij} - \frac{\delta_{ij}}{3}\hat{S}_{p,kk}) + C_I 2\Delta_f^2 \bar{n}_p |\hat{S}_p|^2 \delta_{ij} \ , \qquad (13)$$

where $\hat{S}_p$ is the filtered particle strain rate tensor, $|\hat{S}_p|^2 = 2S_{p,ij}S_{p,ij}$ and Δ_f the filter characteristic length. The model constants have been evaluated in *a priori* tests [69] leading to the values $C_S = 0.02$, $C_I = 0.012$.

3.2.4 Simplified Euler/Euler model

The filtered particle RUE is required twice in the transport equation for filtered particle correlated velocity (Eq. 9): first in the term representing pressure effects due to particle RUE; second when modeling the filtered second-order uncorrelated particle velocity correlation tensor deviatoric (see Eqs. (11) – (12)). To close these two terms, a transport equation for filtered particle RUE can be solved, as proposed by Février *et al.* [32]. This has been done by Kaufmann *et al.* [70] when simulating DNS of particle-laden HIT flows, showing good agreement between Lagrangian and Eulerian results. Still, these models proposed for the unclosed terms due to RUM are very recent and the validity of the viscosity model has recently been questioned by Riber [33] when performing LES in a particle-laden turbulent confined jet flow [71]. Indeed, the resolved particle fluctuations were considerably damped and only the RUM contributed to the particle agitation, which is not realistic. An alternative already tested by Boileau *et al.* [20] and Riber [33], consists in neglecting the RUM contributions in the transport equations for the dispersed phase. Then, the set of equations reduces to:

$$\frac{\partial}{\partial t}\bar{n}_p + \frac{\partial}{\partial x_j}\bar{n}_p\hat{u}_{p,j} = 0 \ , \qquad (14)$$

$$\frac{\partial}{\partial t}\bar{n}_p\hat{u}_{p,i} + \frac{\partial}{\partial x_j}\bar{n}_p\hat{u}_{p,i}\hat{u}_{p,j} = -\frac{\bar{n}_p}{\tau_p}\left(\hat{u}_{p,i} - \hat{u}_{f,i}\right) + \bar{n}_p g_i - \frac{\partial}{\partial x_j}T_{p,ij} \ . \qquad (15)$$

This simplified Euler/Euler model has been chosen to be evaluated in the bluff body configuration. Note that when using this simplified model, the mean particle velocity and mass flux fields are expected to be correctly predicted while the agitation of the particles should be under-estimated since a part, depending on the particle inertia, is the RUM contribution [33].

4 Comparison of single-phase flow simulations

4.1 Choice of the computational domain

The total volume of the configuration is large, due to the length of the ducts (2 m) and the chamber itself (1.5 m), which is far larger than a typical combustion chamber test-rig. Therefore, calculating the whole geometry would be computationally expensive.

Since the location of the second stagnation point mainly depends on the geometry global diameter, the diameters of the inner and annular pipes have been kept: $R_I = 0.010\ m$; $R_{C,1} = 0.075\ m$; $R_{C,2} = 0.150\ m$. In contrast, the pipes have been shortened to 0.1 m for two reasons. On the one hand, it is necessary to decrease the length of the ducts: considering the low Reynolds number and the grid resolution in the inner pipe as well as the accuracy of the numerical scheme, it is impossible to wait for natural destabilisation of the gas flow within the pipe. Specific inlet boundary conditions are therefore used to help the flow destabilisation (see Section 4.3). On the other hand, the pipes cannot be decreased down to 0.1 m: the accurate prediction of particle motion in a pipe (or a channel) is still difficult to obtain, especially because of particle-wall interactions [21] and inter-particle collisions [22]. Since these interactions are not accounted for in this work, one has to ensure that the modified pipe length stays compatible with the particle relaxation time and the particle transit time evaluated in Section 2.2.2.

Note that the length of the chamber (1.5 m) may also be decreased since the second stagnation point is located in the vicinity of $z = 0.4$ m and the flow shows very few structures downstream from this point. In this work, the chamber is shortened for one of the grids tested, as specified in Section 4.2. These simplifications allow to divide the volume of the computational domain by two, which drastically reduces the computational cost of the LES.

4.2 Grids tested

Two grids have been tested on this bluff body configuration to investigate the effects of both resolution and grid type (tetrahedra or hexahedra). Table 3 details the characteristics of the two grids named *gridtet* and *gridhex*. Figures 5 and 6 present an overview of the grid resolutions in longitudinal and front cutting planes respectively.

There are three main differences between the two grids. First, the length of the chamber is different: according to the experimental setup, the chamber is 1.5 m long for *gridtet* whereas *gridhex* has been shortened down to 0.8 m for two reasons. On the one hand, the second stagnation point is located far upstream from the outlet of the chamber. On the second hand, the grid can be easily coarsened downstream from the second stagnation point to save computational cost when using tetrahedra, which is more difficult with hexahedra. This simplification has been verified to have no influence on the results. Consequently, as summarised in Table 3, the total number of cells is very similar for the two grids, but the total volume is twice larger for *gridtet* than for *gridhex*.

The second difference between the two grids deals with the non-dimensional wall distance y^+ in the pipes which is two times smaller in the inner pipe and four times smaller in the coflow in *gridhex* than in *gridtet*. Both grids contain much more cells in the inner pipe than in the outer one. Finally in the tetrahedron-based grid, special care has been taken to generate small cells in the recirculation zones, which was unaffordable in the hexahedron-based grid

considering the increase in computational cost it would induce.

4.3 Boundary conditions

As the two LES codes use different formulations (see Section 3.1), the boundary conditions shown in Fig. 1 are described separately.

4.3.1 Boundary conditions for the AVBP code

The characteristic boundary conditions developed by Poinsot and Lele [72], and Moureau *et al.* [9] are used for these simulations.
The outlet is nearly non-reflective at atmospheric pressure: $P_f = 1.013\ 10^5\ Pa$. The inlet treatment is more complex. Indeed, the first test section where the experimental profiles of mean and fluctuating fluid velocities are known is located at $z = 3\ mm$. Then, the main difficulty consists in specifying the boundary conditions at the inlet of the pipes in order to obtain good agreement between the simulations and the experiments at $z = 3\ mm$. Considering the Reynolds numbers in both pipes (see Section 2.2.1), typical mean axial velocity profiles of fully-developed turbulent pipes (following the classical $1/7$ power-law) are imposed at the inlet of the inner and annular pipes, corresponding to the experimental mass flux. However, the Reynolds numbers in the pipes are too low to expect natural destabilisation of the gas flow, *i.e.*, without any flow forcing. Therefore a time and space-varying velocity signal at the inlet of both pipes is imposed in order to reproduce the effect of an incoming turbulent field as observed in the experiment. This incoming turbulent signal is constructed using a Random Flow Generation (RFG) algorithm [73,74]. The incoming field consists of a superposition of harmonic functions (50 modes projected in the three directions) with two characteristic length-scales prescribed by user: the most energetic length-scale depends on the pipe diameters while the most dissipative one is directly linked to the grid resolu-

tion on the inlet patch. Typical fluctuating profiles of fully-developed pipes are imposed at the inlet of the pipes to match experimental fluctuating profiles at $z = 3\ mm$. Forcing the flow in such a way considerably accelerates the establishment of developed turbulent flows. It also ensures the presence of coherent perturbations not warranted with a pure white noise.
Since the WALE subgrid model shows a correct behavior close to the wall [38], no wall modeling is used: non-slip conditions are imposed at the walls that are isothermal at ambient temperature: $T_f = 293\ K$.

4.3.2 Boundary conditions for the CDP code

An alternative to the RFG method to generate inlet turbulence in the inner pipe is to compute a well-resolved turbulent pipe separately and to inject it in the bluff body computation. The advantage of this injected turbulence is to be non-synthetic without any parameter to prescribe. This method is used for the inner pipe by computing a periodic pipe with a constant volume forcing in the momentum equations. The forcing is dynamically adjusted to obtain the right mass flux. The computational mesh, which is five diameter long, consists of 2.05 million hexahedra with a y^+ equal to 1.9. Even with this well-resolved mesh, the transition from a laminar to a turbulent regime is achieved by beginning the computation with a Reynolds number of 6000 before decreasing slowly to the target Reynolds number of 4500. Then, instead of recording the velocity on a cut plane, a single instantaneous snapshot of the flow is taken. In this snapshot, the streamwise spatial abscissa is transformed into a time abscissa by dividing it by the mean velocity in the pipe. Finally, the inlet velocity for the bluff body pipe is spatially and temporally interpolated from the transformed snapshot. This method saves CPU time because the standalone pipe may be computed during a physical time much shorter than the one needed to converge the bluff body flow. The only drawback is that it deforms

the eddies where the mean streamwise velocity is different of the global mean velocity, mainly close to the wall.
For the coflow, no turbulence is injected. Only the mean velocity profile is prescribed by imposing the experimental mean velocity measured at $z = 3\ mm$. Non-slip conditions are imposed at the walls that are isothermal at ambient temperature: $T_f = 293\ K$ while the outlet is purely convective due to the incompressible equations solved in the CDP code.

4.4 Test cases

In such an industrial-like configuration, the computational cost is often the limiting factor determining the grid resolution and the numerical method to be used. The choice of the numerical scheme (low or high-order), the grid resolution and type (hexahedra or tetrahedra) and the solver type (implicit or explicit) is not straightforward. Whether results are more accurate with a low-order scheme used on a refined grid or with a high-order scheme coupled with a coarser grid is still an open question, for instance [75]. While Colin and Rudgyard [37] and Vreman [76] for example aim at developping high-order schemes on coarse grids, other authors use 2^{nd} order schemes on more refined grids [77,7]. Naturally, the computational cost of the simulation is a key point for the final choice. In this section, five cases are analysed to investigate the influence of:

(1) **the numerical scheme**: the TTGC scheme [4], 3^{rd}-order accurate finite-element, is known to provide better results than the 2^{nd}-order finite-volume LW scheme, especially in recirculating flows. The influence of the scheme is shown in Section 4.6 using the same unstructured grid *gridtet*, and the AVBP code.
(2) **the inlet boundary condition treatment:** the relatively low Reynolds number associated with a low grid resolution in the pipes do not allow a

natural transition to turbulence. The influence of the inlet forcing using the RFG method described in Section 4.3.1, is analysed in Section 4.7 using the AVBP code with the grid *gridtet* and the TTGC scheme.

(3) **the grid:** hexahedron-based grids are rarely used to calculate swirled flows since they are said to generate preferential directions. The AVBP code with the TTGC scheme is used to investigate the influence of grid type and grid resolution in Section 4.8.

(4) **the code:** in Section 4.10, the results provided by AVBP and CDP on the hexahedron-based grid *gridhex* are compared with the measurements to evaluate the accuracy of both gas LES solvers.

All cases are summarised in Table 4 for those carried out with AVBP whereas the LES performed with CDP is detailed in Section 4.10. To validate results, the following diagnostics are used:

(1) the Q-criterion of Dubief and Delcayre [78], Hunt *et al.* [79] and Hussain and Jeong [80] to visualise the flow structures;

(2) the axial variations of mean and root-mean-square (RMS) axial velocities (as plotted in Fig. 3 in Borée *et al.* [1]) to measure the length of the recirculation zone;

(3) the radial variations of mean and RMS axial velocities at seven stations along the duct axis ($z = 3, 80, 160, 200, 240, 320$ and 400 mm as represented in Fig. 7) to provide a detailed comparison of LES and experimental fields.

The cylindrical coordinate system (z, r, θ) is used to indicate axial (downward), radial and azimuthal directions. As no mean swirling motion was detected, only the axial and radial velocity components are provided. The mean components resulting from LES-averaging are respectively noted W and U_r whereas the RMS components are w_{rms} and $u_{r,rms}$.

The analysis of the averaged quantities resulting from LES requires a simulation time long enough to ensure convergence, and a sampling time small enough to ensure that the smallest structures can contribute to the averaged solution. In the present configuration, the lowest frequency to be represented is associated to the two counter-rotating structures on each side of the axis as plotted in Fig. 2 c. Considering their size $l_{f,l} \approx 8.10^{-2}\ m$, and their mean rotating velocity $U_{f,l} \approx 1\ m.s^{-1}$, the order of magnitude of the associated time is $\tau_{f,l} \approx 8.10^{-2}\ s$. The most energetic eddies in the inner pipe constitute a reasonable choice to determine the order of magnitude of the highest frequencies. Considering their size $l_{f,t} \approx 7.10^{-3}\ m$, and their velocity $u'_{f,t} \approx 1.5\ m.s^{-1}$, the order of magnitude of the associated time-scale is $\tau_{f,t} \approx 4.6\ 10^{-3}\ s$. All the LES performed with the explicit solver AVBP have been run for $T_{av,AVBP} \approx 1\ s$ while the LES performed with the implicit solver CDP has been run longer: $T_{av,CDP} \approx 2.5\ s$. The time between two samples is $\Delta t_r \approx 1.2\ 10^{-3}\ s$. In both codes, the statistics of the mean fields are then well converged. This is not always the case for the RMS quantities but the overall tendency gives enough information to compare models and solvers.

Figure 7 shows an instantaneous field of the gas velocity modulus in the cutting plane $y = 0$ for the case *avbp_hex_ttgc_rfg*. Many structures of different sizes are visible. The largest ones are linked to the diameter of the coflow, intermediate ones appear in the shear layers and structures coming out of the inner jet are also clearly identified.

The time-averaged fields considerably differ from the instantaneous flow structure. Figures 8 a. – c. present, respectively, the mean field of gas axial velocity, and the RMS fields of gas axial and radial velocities in the cutting plane $y = 0$ for the case *avbp_hex_ttgc_rfg*. The iso-contour line of zero mean axial ve-

locity is added on the three pictures. All fields are rather symmetric, which indicates good convergence of the simulations. As expected, there are two points with zero velocity along the axis, corresponding to distinct inner jet and coflow stagnation points. The peak of axial fluctuations is located at the inner jet stagnation point whereas the radial fluctuations are maximum in the vicinity of the furthest stagnation point. Both axial and radial fluctuations show secondary peaks, respectively in the external shear layer and close to the first stagnation point. At these two specific locations, turbulence is highly anisotropic.

4.6 Influence of the numerical scheme

To evaluate the influence of the numerical scheme on the gas flow, the cases *avbp_tet_lw_norfg* and *avbp_tet_ttgc_norfg* are compared. Both LES are performed with AVBP on the unstructured grid *gridtet*. The RFG method is not used at the inlet of the ducts so that the only difference between the two cases is the numerical scheme.

The qualitative impact of the scheme order on the small structures is clear on Fig. 9 where instantaneous iso-surfaces of Q-criterion are displayed for both LW and TTGC schemes. Both fields exhibit two kinds of coherent structures: some longitudinal vortices come from the inner pipe whereas some others are created in the external shear zone and are rather azimuthal. However, the TTGC scheme provides more numerous and more detailed flow structures than the LW scheme.

These differences are quantified in Fig. 10 where the axial profiles of mean and RMS axial velocities are plotted. When using LW, the two points with zero mean axial velocity that delimit the recirculation zone are located too far downstream from the ducts, and so is the peak of RMS axial velocity. On

the contrary, the location of the two stagnation points as well as the peak of RMS axial velocity are well predicted with TTGC. Only the amplitude of this peak is over-estimated. With two-phase flows and even combustion in prospect, delimiting precisely the recirculation zone is of high importance: the particle distribution as well as the flame location and shape greatly depend on the first stagnation point. Consequently, all the LES performed with AVBP and analysed hereafter use the TTGC scheme.

4.7 Influence of the inlet boundary treatment

The runs of Fig. 10 were performed without imposing turbulent velocity fluctuations in the inner pipe and this simplification is questionable. Indeed, the mean axial fluid velocity is shown to increase along the inner pipe ($-0.1 < z < 0$) while there is no fluctuation developing in the duct, showing that the turbulent flow within the central pipe is not correctly captured by the solver. Performing a true LES in the ducts would be computationaly expensive because it would require a considerable increase in resolution. Therefore in this work, the specific inlet boundary treatment described in Section 4.3.1 has been used to feed turbulent fluctuations in the inner pipe.

The direct comparison of the cases *avbp_tet_ttgc_norfg* and *avbp_tet_ttgc_rfg* exhibits the impact of the inlet turbulent forcing method, as shown in Fig. 11. Usually in a pipe flow, the peaks of velocity fluctuations reach almost 10 % of the mean velocity on the centerline. Owing to a lack of resolution in the inner pipe, the velocity fluctuations imposed at the inlet of the pipe have deliberately been increased to 15 % of the axial mean velocity. The main purpose is to get good agreement between simulations and experiments at the outlet of the duct, i.e., at $z = 3\ mm$, which is shown in Fig. 11 b. The consequence of the fluid agitation in the duct itself is a flatter mean axial velocity profile in the pipe: Fig. 11 a. shows that the maximum of mean axial velocity is in

better agreement with the experiments at the outlet of the duct when using the RFG method. Note that the accurate prediction of the location of the recirculation zone for the case *avbp_tet_ttgc_norfg* is only due to a fortuitous compensation of errors.

4.8 Influence of the grid

The influence of the grid type as well as the grid resolution is investigated comparing the results provided by the cases *avbp_tet_ttgc_rfg* and *avbp_hex_ttgc_rfg*. As mentioned in Table 4, the only difference between these two LES is the grid.

The qualitative impact of the grid on the fluid flow topology is shown in Fig. 12 where instantaneous iso-surfaces of Q-criterion are displayed for both cases. Although the two fields exhibit the same kind of longitudinal and azimuthal coherent stuctures, there are much more, but also much smaller vortices with the hexahedron-based grid. In other words, both grids resolve the large vortices in the same way but the grid *gridhex* resolves much smaller eddies whereas they are dissipated by the grid *gridtet*.

Nevertheless, these differences in flow structures are difficult to quantify when plotting the radial mean and RMS axial velocity at the seven experimental stations as done in Fig. 13. The amplitude of the mean and RMS velocity is very similar for both grids, and in good agreement with the measurements. The most significant discrepancy is located in the central region close to the station $z = 80\ mm$ where the axial velocity fluctuations are over-estimated with *gridtet*. As a consequence, the inner jet flow penetrates slightly farther in the chamber, improving the prediction of the location of the first stagnation point as well as the length of the recirculation zone.

4.9 Compromise between scheme order and grid

Accounting for the cost efficiency slightly modifies the conclusions drawn in Section 4.6 and 4.8. Table 5 compares the computational cost of the cases *avbp_tet_lw_norfg*, *avbp_tet_ttgc_rfg* and *avbp_hex_ttgc_rfg* when simulating 0.1 *s* physical time. Note that the RFG inlet treatment does not notably modify the computational cost so that the case *avbp_tet_ttgc_norfg* is not reported in Table 5. On the one hand, the computational cost of a simulation with TTGC is 2.5 bigger than with LW [4]. On the other hand, using the unstructured grid *gridtet* is about four times cheaper than using the hexahedron-based grid *gridhex*. This figure is to be related to the gain in quality of the predictions choosing the final configuration and grid.

4.10 Influence of the code

The accuracy of both AVBP and CDP codes is finally compared analysing the results provided by the cases *cdp_hex* and *avbp_hex_ttgc_rfg*. For this purpose, the case *avbp_hex_ttgc_rfg* has been chosen, not only because it shows the best agreement with the measurements but also because it is the best candidate for direct comparisons with CDP. Indeed, both codes use here the same hexahedron-based grid. There are however some differences in the parameters used, as summarised in Table 6. As already mentioned, CDP solves the incompressible Navier-Stokes equations implicitly whereas AVBP solves the compressible Navier-Stokes equations explicitly. The main consequence is that the time step is 35 times larger for CDP, leading to a reduced computational cost. As a result, the total averaging time is smaller for AVBP, but the convergence has been ensured to be good enough. Another noticeable difference is the treatment of the inlet boundary condition, as detailed in Section 4.3.

Figure 14 displays mean and RMS gas axial velocities along the axis while Fig. 15 shows the radial profiles of mean and RMS gas axial velocities for the two codes along with the experimental measurements. The global agreement between the two codes and the experiments is very good and most of the flow physics is captured by the two LES codes. The width and the length of the recirculation zone are well predicted (see Fig. 15 a.). As shown in Fig. 14 a., the differences between both codes in predicting the location of the two stagnation points are minor. Focusing on the RMS velocities in Fig. 15 b., the agreement with measurements is also good. The location and the amplitude of the peaks are well predicted, except in the coflow where CDP underpredicts the RMS velocities. The origin of the discrepancy is the treatment of the coflow inlet boundary condition, with no turbulence injected with CDP in the outer duct.

The overall result is that both codes provide very similar results, also close to the measurements, even though they use different numerical methods. This indicates that the accuracy of both codes is good enough to test the dispersed phase with reasonable confidence on this configuration.

5 Comparison of two-phase flow simulations

This section presents the results for the 22 % particle mass loading ratio of the central jet. Riber [33] showed that the impact of the dispersed phase on the gas phase is limited at this mass loading ratio: the central jet penetrates slightly further in the chamber, also slightly modifying the location of the recirculation zone. As the differences with the single-phase flow case are minor in the present case, the gas phase results are not discussed and only the results for the dispersed phase are provided hereafter. The validation of the particle dynamics modeling in this recirculating gas flow is done using three different solvers: CDP and AVBP-EL which both calculate the particle motion with

the EL approach summarised in Section 3.2.1, and AVBP-EE that uses the simplified mesoscopic EE approach detailed in Section 3.2.2.
An essential part of these two-phase flow LES is the introduction of particles in terms of position and velocity in the central jet. This point is discussed in Section 5.1. Then, the three solvers are compared in two steps in Section 5.2. First, since the gas LES solvers from AVBP and CDP give very similar results on the hexahedron-based grid *gridhex*, the two Lagrangian solvers CDP and AVBP-EL are compared and validated by comparisons with the measurements. Second, the two approaches (EL and mesoscopic EE) are compared using the solvers AVBP-EL and AVBP-EE on *gridhex*. As the gas solver and the grid are exactly the same, a direct comparison of the two methods is proposed.

5.1 Particle injection and test cases

In all cases, the injected particles have a diameter of 60 μm, as justified in Section 2.3. The introduction of these particles in terms of position and velocity is one of the main difficulty in such a two-phase flow configuration. First, the methodology differs depending on the solver used. Second, the injection planes are different for all solvers, as shown in Fig. 16. Thus, the impact of the particle injection method on the results can be evaluated. In AVBP-EE, both the particle number density profile and the mean velocity profile are imposed at the inner pipe inlet ($z = -100\ mm$) and correspond to the ones measured experimentally at $z = 3\ mm$. No turbulent fluctuations are introduced. In AVBP-EL and in CDP, the injection planes are located at $z = -3\ mm$ and $z = -95\ mm$ respectively. The injection speed profile is also the experimental one measured at $z = 3\ mm$ but the mass loading is homogeneous over the injection section. Furthermore in AVBP-EL and in CDP, a white noise (amplitude of the order of 10 % of the mean velocity) is added to the particle mean velocity profiles to match experimental measurements at $z = 3\ mm$.

These differences in particle injection are summarised in Table 7. Although they must be taken into account when comparing the three solvers AVBP-EL, AVBP-EE and CDP, the comparison of the Lagrangian solvers on the one hand, and the EL and mesoscopic EE approaches on the other hand is still relevant. The three LES performed with the three different solvers are also detailed in Table 7. The case *cdp_EL_hex* uses the same gaseous parameters as the case *cdp_hex* whereas the two cases *avbp_EL_hex* and *avbp_EE_hex* are based on the case *avbp_hex_ttgc_rfg* (see Table 6). Due to the implicit formulation of CDP, the total averaging time affordable with CDP is once again larger than with AVBP.

5.2 Results for two-phase flow simulations

Figures 17 – 18 display the radial profiles of mean and RMS axial and radial particle velocities at the seven stations along the axis while Fig. 19 shows the axial profiles of mean and RMS axial particle velocities. The results of the three cases defined in Table 7 are directly compared with measurements. For the sake of simplicity, the analysis of the results is divided into two parts: first, the Lagrangian solvers are compared in Section 5.2.1. Second, the EL and mesoscopic EE approaches are directly compared in Section 5.2.2.

5.2.1 Comparison of the two EL solvers

Focusing on the results obtained with the two Lagrangian solvers, Figs. 17 – 19 show a very good agreement between the two codes, and with the measurements. Better results are generally obtained with CDP but not in all sections. A convenient way to look at the results is to consider the central axis of the configuration: a critical zone is located around $z = 160\ mm$, the stagnation point for the gas phase. This is also a zone where particles accumulate and must stop before turning around to escape from the recirculating zone by the

sides. As a consequence, this zone is difficult to predict accurately for the dispersed phase and the slight differences in calculating the turbulence in the inner pipe may induce such discrepancies on the dispersed phase.

5.2.2 Comparison of the EL and the EE approaches

In this section, the cases *avbp_EL_hex* and *avbp_EE_hex* are compared. As the two cases use the same grid and exactly the same gas solver, the EL approach and the mesoscopic EE approach can be directly compared.

First, a qualitative comparison is provided in Fig. 20 which displays instantaneous fields of particle number density for the two cases. Note that this quantity is directly available when using the mesoscopic EE approach but is reconstructed from the Lagrangian simulations using a volumic projection method. The two instantaneous fields of particle number density are similar: both approaches show several of particles along the inner jet and the largest one is located close to the second stagnation point. Most of the particles trapped in this region are then released in the gaseous recirculation zones. The two fields show however differences when focusing on the small structures which are more numerous using the EL approach.

Second, Figs. 17 – 19 show that the two approaches provide extremely similar results showing that the mesoscopic EE approach is able to compute such a flow and to provide results that are equivalent in precision to an EL computation. There are however at least two discrepancies. First, the mean particle axial velocity profiles at $z = 160\ mm$ show that the particles do not go far enough in the chamber with the mesoscopic EE approach. Nevertheless, this point has been shown to be very delicate to predict for the gas phase and very dependent on the inlet conditions in the pipe. In the present EE computation, no particle velocity fluctuations are imposed at the inlet of the inner pipe with the mesoscopic approach but this may not be crucial. The second main difference deals with the particle agitation that is under-estimated by the

mesoscopic EE approach both on the radial and the axial profiles of particle RMS velocities. Actually, this is not surprising since the simplified mesoscopic EE model is used in this work: as the total particle agitation is divided into a correlated and an uncorrelated part, neglecting the RUM contribution in this bluff body flow prevents from predicting the experimental level of particle agitation. Nevertheless, the mean quantities are still well predicted with the mesoscopic EE model.

5.2.3 Scalability of the EL approach

One interesting issue in the comparison between Eulerian and Lagrangian methods is the analysis of scalability and computational performance. The implementation on massively parallel machines of the Eulerian approaches is not technically problematic because the flow and the droplets are solved on the same grid using the same spatial discretization scheme. On the other hand, Lagrangian approaches are less well-suited to parallel computers since the two phases must be coupled, which increases the complexity of the implementation. Thus, before implementing a Lagrangian module into a new solver one of these two strategies should be adopted for the dispersed phase treatment:

(1) Task parallelization in which some processors compute the gaseous phase and others compute the droplets.
(2) Domain partitioning in which particles are computed together with the gas flow on geometrical subdomains mapped on parallel processors. Individual particles or parcels are tracked as they cross the computational domain and must be exchanged between processors when leaving a subdomain to enter an adjacent one.

Particle tracking within an unstructured solver reveals an additional constraint since particle coordinates can not be easily used to locate them inside a cell, and time (and memory) consuming searching algorihtm must be used. How-

ever, for LES it is easy to show that only the strategy based on domain partitioning is efficient on large grids because task parallelization would require the communication of very large three-dimensional data sets at each iteration between all processors. It is well known that codes based on domain partitioning are difficult to optimize on massively parallel architectures when droplets are clustered in one part of the domain (typically, near the fuel injectors) due to load imbalance. Moreover, the distribution of droplets may change during the computation: for a gas turbine reignition sequence, for example, the chamber is filled with droplets when the ignition begins thus ensuring an almost uniform droplet distribution; these droplets then evaporate rapidly during the computation, leaving droplets only in the near injector regions. This may lead to a poor speedup on a parallel machine if the domain is decomposed in the same way for the entire computation since some processors should compute a high number of particles while other are waiting for this task to finish. As a result, load balancing strategies are required to redecompose the domain by taking into account particles information to preserve a high parallel efficiency [14].

In this section, the scalability of the AVBP-EL solver is analyzed using the simulation speedup and the reference single-phase CPU time ratio. The former is defined as the ratio between the CPU time of a simulation with n processors and the CPU time of a simulation with a given number of processors, N_{procs}:

$$Speedup = \frac{T_{run}(n)}{T_{run}(N_{procs})} * n \ . \tag{16}$$

The latter is defined as the ratio between the CPU time of a simulation with a given number of processors and the CPU time of the reference single-phase simulation with n processors:

$$CPU\ time\ ratio = \frac{T_{run}(N_{procs})}{T_{single-phase}(n)} \ . \tag{17}$$

Default value of n is 1 but sometimes it is not possible to run the sequential simulation mainly due to high memory requirements, in which case the

speedup and CPU time ratio are reported to a reference parallel simulation. This scalability study has been performed in a CRAY XD1 [2] supercomputer for a number of processors up to 64. Results of the moderate mass loading test case for the two grids named *gridtet* and *gridhex* are presented hereafter. The total number of particles presented in the domain is of the order of 560,000 and 430,000, respectively. Variations smaller than 0.5 % in the number of particles were observed between the beginning and the end of the simulation, which implies that it is statistically stationary. The lower number of particles used in *gridhex* is due to the difference in the length between the two grids (see Table 3). Even if the length of the chamber is half the dimension of *gridtet*, the number of particles is three-fourths since they are mainly concentrated inside the recirculation zone.

Figure 21 shows the speedup of the single-phase and the monodisperse test case with *gridtet* (Fig. 21 a.) and *gridhex* (Fig. 21 b.) using AVBP-EL. Scaling of *gridhex* is reported relative to the 8 processor case ($n = 8$), which was the smallest number of CRAY XD1 processors that could run this problem due to high memory requirements. In both cases, the good scalability of the single-phase is unquestionable. The drop of performances observed in Fig. 21 a. for the two-phase flow simulation is not related to large communications costs between processors but merely to the parallel load imbalance generated by the partitioning algorithm [15]. The same simulation with a different grid can lead to a completely different speedup graph, as it can be observed from Fig. 21 b. Note that these graphs do not contain information about the speedup with AVBP-EE. It can be considered as good as the single-phase computation since the dispersed phase uses the same parallelization applied to the gaseous phase.

The differences between the two speedup graphs can be explained by plotting the number of nodes (or cells) and particles presented in each processor. As AVBP is based on a *cell-vertex* formulation, comparing the number of nodes

[2] This machine has 58 nodes with 2 processors/node and 2 GB/processor.

to the number of particles is more representative of the computational loading since almost all arrays are dimensioned as a function of the number of nodes per processor. Figure 22 reports the number of nodes and particles per processor for a 32-partition simulation by using a recursive inertial bisection (RIB) [81] partitioning algorithm, with *gridtet* and *gridhex*, respectively. As expected from Fig. 21, Fig. 22 shows an excellent load-balancing for the gaseous phase: all processors contain about the same number of nodes. On the contrary, it shows a strong particle load imbalance (Fig. 22 a.) where one single processor contains almost half the total number of particles of the simulation. This fact is related to the grid downstream coarsening which increases significantly the memory requirements and the floating-point operations for this processor. This points out the need of load balancing strategies for two-phase flow simulations with a Lagrangian approach, for example, by using multi-constraint partitioning algorithms which take into account particle loading on each processor [14]. Even if the dispersed phase presents a small load imbalance in Fig. 22 b., it is hidden by the higher computational loading needed to calculate the gaseous phase. This is the main reason of the good speedup observed in Fig. 21 b.

Tables 8 and 9 summarized the CPU time ratios of AVBP-EL with both grids on a CRAY XD1 supercomputer. Additional time to perform the two-phase flow simulation can vary from 5 % up to 87 % with the Lagrangian formulation in *gridtet* but it is not higher than 5 % with *gridhex* which confirms the tendencies observed with the speedup graphs. All simulations with AVBP-EE has a constant added cost of the order of 80 % since this approach is independent of the mass loading. Therefore, at this moderate mass loading the Lagrangian approach proved to be faster than the Eulerian formulation.

The previous results require additional comments:

- The quality of the gas phase prediction is essential for the dispersed phase results.
- The comparison of different solvers and boundary conditions demonstrates the importance of the flow in the central injection pipe: the mean and RMS gas velocity profiles as well as the particle motion directly change the flow field significantly. For example, the location of the stagnation points (see Fig. 14) is extremely sensitive to any change in the inlet pipe boundary conditions. This is a major drawback of this configuration because performing an accurate LES of the two-phase flow within this pipe is still out of reach of present capacities for at least two reasons. First, the gaseous flow within the pipe is difficult to resolve and would require a very fine mesh and sophisticated wall models. Second, the two-phase flow in the pipe is heavily loaded so that computing the motion of the particles within the pipe would require additional models for particle-particle and wall-particle interactions [35]. For the present results, the boundary conditions for the dispersed phase at the tube inlet are approximate solutions and the variety of methods tested for the LES of Table 7 demonstrates that no easy solution was found to model particles injection in the central tube.

Despite these limitations and differences in inlet conditions, results confirm that most of the flow structures are correctly captured and that LES of two phase flows (using EL or mesoscopic EE approaches) is possible and provides accurate results. To improve on these results, a significant effort will have to be applied to describe the two-phase flow within the injection tube. Note that in a real combustion chamber, the region where such heavily loaded flows are found is very small and limited to the vicinity of the fuel injector.

6 Conclusions

This work has presented a comparison between multiple LES approaches and codes for non-reacting two-phase flows and the experimental results of Borée *et al.* [1]. This experiment was chosen because it contains multiple complex flow features which are typical of combustion chambers: strong recirculating zones created by a dump geometry, multiple stagnation points, high turbulent Reynolds number. LES and experiments have been compared in terms of radial profiles of mean and RMS axial and radial velocities at seven stations along the axis, and axial profiles of mean and RMS axial velocities on the experiment central axis. LES approaches included both Euler/Euler and Euler/Lagrange models. Two codes (incompressible implicit and compressible explicit) were used to evaluate the effects of the gas solver on the results so that three two-phase flow solvers were used:

- an Euler/Euler explicit compressible solver;
- an Euler/Lagrange explicit compressible solver;
- an Euler/Lagrange implicit incompressible solver.

All computations were performed for monodisperse particle distributions with diameter $d_p = 60\ \mu m$ which corresponds to the initial mean experimental diameter in mass. The effects of subgrid-scale model, numerical scheme accuracy and of grid refinement were also investigated. The main conclusions are the following:

- All LES approaches provide high-quality results compared to the PDA data of the configuration of Borée *et al.* [1], thereby confirming the potential of these methods and their relative insensitivity to the details of the numerical solver. The variations between LES solvers are mainly due to changes in boundary conditions.
- The quality of the gas flow predictions is critical in order to accurately

compute the dispersed phase.

- The most critical parameter controlling accuracy is the grid and the convective scheme: using high-order schemes built for LES provides the best results.
- The most critical zone in the flow is the central injection tube which feeds the experiment with a highly loaded air/particles jet. True two-phase LES is impossible in this duct today. Results show that this element controls the flow, especially the positions of stagnation points on the experiment axis. Even though the quality of the present LES results is high in most of the flow, this work confirms that future LES accuracy in combustion chambers will need to include all feeding ducts which represents a significant challenge.
- Both Euler/Lagrange codes provide very similar results while the Euler/Euler approach gives similar mean velocity fields but slightly understimates fields of particle agitation. This corresponds to the expected behavior of the present mesoscopic model in which the uncorrelated motion was not taken into account [32,33].
- For the present case with moderate mass loading, the total number of particles per processor is moderate. The CPU and memory requirements to track particles is lower than for the gaseous phase even with the load balancing problem observed with one of the grids studied. Although the additional cost of Eulerian formulations is independent of the mass loading, for such a dilute case, the Lagrangian approach proved to be faster up to 64 processors.

These results confirm the potential of LES approaches for two-phase flows. Nevertheless, there is still much work to be done concerning:

- the effects of the subgrid fluid turbulence on the particle velocity [53];
- the RUM modeling in order to estimate the particle agitation more precisely with the mesoscopic EE approach;
- the wall-particle interactions as well as the particle-particle interactions to simulate the dispersed phase accurately in pipe and channel flows;

- the extension to two-phase reacting flows which has already been initiated [20].

7 Acknowledgements

Part of this work was performed during the 2006 CTR Summer Program at Stanford and the support of Pr Pitsch and Moin is gratefully acknowledged. Most simulations were performed on the national computing center CINES in Montpellier and on CTR supercomputers.

References

[1] J. Borée, T. Ishima, I. Flour, The effect of mass loading and inter-particle collisions on the development of the polydispersed two-phase flow downstream of a confined bluff body, J. Fluid Mech. 443 (2001) 129–165.

[2] D. Caraeni, C. Bergstrom, L. Fuchs, Modeling of liquid fuel injection, evaporation and mixing in a gas turbine burner using Large Eddy Simulation, Flow, Turb. and Combustion 65 (2000) 223–244.

[3] V. Chakravarthy, S. Menon, Subgrid modeling of turbulent premixed flames in the flamelet regime, Flow, Turb. and Combustion 65 (2000) 133–161.

[4] O. Colin, F. Ducros, D. Veynante, T. Poinsot, A thickened flame model for large eddy simulations of turbulent premixed combustion, Phys. Fluids 12 (7) (2000) 1843–1863.

[5] H. Forkel, J. Janicka, Large eddy simulation of a turbulent hydrogen diffusion flame, Flow, Turb. and Combustion 65 (2) (2000) 163–175.

[6] H. Pitsch, L. Duchamp de la Geneste, Large eddy simulation of premixed turbulent combustion using a level-set approach, Proc. of the Comb. Institute 29 (2002) 2001–2005.

[7] K. Mahesh, G. Constantinescu, P. Moin, A numerical method for large eddy simulation in complex geometries, J. Comput. Phys. 197 (1) (2004) 215–240.

[8] L. Selle, G. Lartigue, T. Poinsot, R. Koch, K.-U. Schildmacher, W. Krebs, B. Prade, P. Kaufmann, D. Veynante, Compressible large eddy simulation of turbulent combustion in complex geometry on unstructured meshes, Combust. Flame 137 (4) (2004) 489–505.

[9] V. Moureau, G. Lartigue, Y. Sommerer, C. Angelberger, O. Colin, T. Poinsot, High-order methods for DNS and LES of compressible multi-component reacting flows on fixed and moving grids, J. Comput. Phys. 202 (2) (2005) 710–736.

[10] S. Roux, G. Lartigue, T. Poinsot, U. Meier, C. Bérat, Studies of mean and unsteady flow in a swirled combustor using experiments, acoustic analysis and large eddy simulations, Combust. Flame 141 (2005) 40–54.

[11] T. Poinsot, D. Veynante, Theoretical and numerical combustion, R.T. Edwards, 2nd edition., 2005.

[12] P. Schmitt, T. Poinsot, B. Schuermans, K. Geigle, Large eddy simulation and experimental study of heat transfer, nitric oxide emissions and combustion instability in a swirled turbulent high pressure burner, J. Fluid Mech. 570 (2007) 17–46.

[13] G. Staffelbach, L. Gicquel, T. Poinsot, Highly parallel large eddy simulations of multiburner configurations in industrial gas turbines, Lecture Notes in Computational Science and Engineering - Complex effects in Large Eddy Simulation 56 (2006) 326–336.

[14] F. Ham, S. Apte, G. Iaccarino, X. Wu, M. Herrmann, G. Constantinescu, K. Mahesh, P. Moin, Unstructured LES of reacting multiphase flows in realistic gas turbine combustors, in: Annual Research Briefs, Center for Turbulence Research, NASA Ames/Stanford Univ., 2003, pp. 139–160.

[15] M. García, Y. Sommerer, T. Schönfeld, T. Poinsot, Evaluation of Euler-Euler and Euler-Lagrange strategies for large-eddy simulations of turbulent reacting

flows, in: ECCOMAS thematic conference on computational combustion, Lisbon, Portugal, 2005.

[16] L. Chin, R. Tankin, Vortical structures from a two-dimensional nozzle with a bluff body slot, Phys. Fluids A 4 (8) (1992) 1724–1736.

[17] R. Schefer, M. Namazian, J. Kelly, Velocity measurements in turbulent bluff body stabilized flows, AIAA Journal 32 (9) (1994) 1844–1851.

[18] M. Namazian, J. Kelly, R. Schefer, Concentration imaging measurements in turbulent concentric-jet flows, AIAA Journal 30 (1992) 384–394.

[19] Y. Hardalupas, C. Liu, J. Whitelaw, Experiments with disk stabilised kerosene-fuelled flames, Combust. Sci. Tech. 97 (1994) 157–191.

[20] M. Boileau, S. Pascaud, E. Riber, B. Cuenot, L. Gicquel, T. Poinsot, Large eddy simulation of spray combustion in gas turbines, Flow, Turb. and Combustion 80 (2008) 351–373.

[21] Q. Wang, K. Squires, Large eddy simulation of particle-laden turbulent channel flow, Phys. Fluids 8 (5) (1996) 1207–1223.

[22] M. Vance, K. Squires, O. Simonin, Properties of the particle velocity field in gas-solid turbulent channel flow, Phys. Fluids 18 (063302).

[23] M. Picciotto, C. Marchioli, A. Soldati, Characterization of near-wall accumulation regions for inertial particles in turbulent boundary layers, Phys. Fluids 17 (098101).

[24] C. Marchioli, M. Picciotto, A. Soldati, Particle dispersion and wall-dependent fluid scales in turbulent bounded flow: Implications for local equilibrium models, J. of Turb. 7 (60) (2006) 1–12.

[25] M. Sakiz, O. Simonin, Development and validation of continuum particle wall boundary conditions using Lagrangian simulation of a vertical gas-solid channel flow, in: Proc. 8^{th} Int. Symp. on Gas-Particle Flows, ASME Fluids Engineering Division Summer Meeting, Vol. FEDSM99-7898, 1999.

[26] V. Alipchenkov, L. Zaichik, O. Simonin, A comparison of two approaches to derivation of boundary conditions for continuous equations of particle motion in turbulent flow, High Temperature, Translated from Teplofizika Vysokikh Temperatur 39 (2001) 108–114.

[27] O. Simonin, J. He, Eulerian prediction of the particle behaviour in a turbulent boundary layer, in: Proc. 6th Workshop on Two-Phase Flow Predictions, Erlangen 1992, M. Sommerfeld (Editor), Bilateral Seminars of the International Bureau / Forschungszentrum Juelich GmbH, Vol. 14, Erlangen, Germany, 1993, pp. 154–165.

[28] G. Desoutter, B. Cuenot, C. Habchi, T. Poinsot, Interaction of a premixed flame with a liquid fuel film on a wall, Proc. of the Combustion Institute 30 (2005) 259–266.

[29] W. Bachalo, M. Houser, Phase/doppler spray analyser for simultaneous measurements of drop size and velocity distributions, Opt. Eng. 23 (1984) 583–590.

[30] R. W. Schefer, M. Namazian, J. Kelly, Stabilization of lifted turbulent-jet flames, Combust. Flame 99 (1994) 75–86.

[31] A. Kaufmann, O. Simonin, B. Cuenot, T. Poinsot, J. Hélie, Dynamics and dispersion in 3D unsteady simulations of two phase flows, in: Supercomputing in Nuclear Applications, CEA, Paris, 2003.

[32] P. Février, O. Simonin, K. Squires, Partitioning of particle velocities in gas-solid turbulent flows into a continuous field and a spatially uncorrelated random distribution: Theoretical formalism and numerical study, J. Fluid Mech. 533 (2005) 1–46.

[33] E. Riber, Développement de la méthode de simulation aux grandes échelles pour les écoulements diphasiques turbulents, Phd thesis, INP Toulouse (2007).

[34] R. Fan, D. L. Marchisio, R. O. Fox, Application of the direct quadrature method of moments to polydisperse gas-solid fluidized beds, Powder and Technology 139 (7) (2004).

[35] N. Caraman, J. Borée, O. Simonin, Effect of collisions on the dispersed phase fluctuation in a dilute tube flow: experimental and theoretical analysis, Phys. Fluids 15 (12) (2003) 3602–3612.

[36] F. Ham, G. Iaccarino, Energy conservation in collocated discretization schemes on unstructured meshes, in: Annual Research Briefs, Center for Turbulence Research, NASA Ames/Stanford Univ., 2004, pp. 3–14.

[37] O. Colin, M. Rudgyard, Development of high-order taylor-galerkin schemes for unsteady calculations, J. Comput. Phys. 162 (2) (2000) 338–371.

[38] F. Nicoud, F. Ducros, Subgrid-scale stress modelling based on the square of the velocity gradient, Flow, Turb. and Combustion 62 (3) (1999) 183–200.

[39] J. Kim, P. Moin, Application of a fractional-step method to incompressible Navier-Stokes equations, J. Comput. Phys. 59 (2) (1985) 308–323.

[40] M. Germano, U. Piomelli, P. Moin, W. Cabot, A dynamic subgrid-scale eddy viscosity model, Phys. Fluids 3 (7) (1991) 1760–1765.

[41] M. Maxey, The gravitational settling of aerosol particles in homogeneous turbulence and random flow fields, J. Fluid Mech. 174 (1987) 441–465.

[42] R. Gatignol, The Faxén formulae for a rigid particle in an unsteady non-uniform Stokes flow, Journal de mécanique théorique et appliquée 1 (2) (1983) 143–160.

[43] M. Boivin, O. Simonin, K. Squires, Direct numerical simulation of turbulence modulation by particles in isotropic turbulence, J. Fluid Mech. 375 (1998) 235–263.

[44] O. Vermorel, B. Bédat, O. Simonin, T. Poinsot, Numerical study and modelling of turbulence modulation in a particle laden slab flow, J. of Turb. 4, 025.

[45] S. Elghobashi, G. Truesdell, On the two-way interaction between homogeneous turbulence and dispersed solid particles, Phys. Fluids 5 (7) (1993) 1790–1801.

[46] K. Squires, J. Eaton, Particle response and turbulence modification in isotropic turbulence, Phys. Fluids 2 (7) (1990) 1191–1203.

[47] R. Miller, J. Bellan, Direct numerical simulation and subgrid analysis of a transitional droplet laden mixing layer, Phys. Fluids 12 (3) (1999) 650–671.

[48] M. Boivin, O. Simonin, K. Squires, On the prediction of gas-solid flows with two-way coupling using large eddy simulation, Phys. Fluids 12 (8) (2000) 2080–2090.

[49] L. Schiller, A. Nauman, A drag coefficient correlation, VDI Zeitung 77 (1935) 318–320.

[50] M. Maxey, J. Riley, Equation of motion for a small rigid sphere in a nonuniform flow, Phys. Fluids 26 (4) (1983) 883–889.

[51] Y. Yamamoto, M. Potthoff, T. Tanaka, T. Kajishima, Y. Tsuji, Large-eddy simulation of turbulent gas-particle flow in a vertical channel: effect of considering inter-particle collisions, J. Fluid Mech. 442 (2001) 303–334.

[52] S. Apte, K. Mahesh, T. Lundgren, A Eulerian-Lagrangian model to simulate two-phase particulate flows, in: Annual Research Briefs, Center for Turbulence Research, NASA Ames/Stanford Univ., 2003, pp. 161–167.

[53] P. Fede, O. Simonin, Numerical study of the subgrid fluid turbulence effects on the statistics of heavy colliding particles, Phys. Fluids 18 (045103).

[54] O. Druzhinin, S. Elghobashi, On the decay rate of isotropic turbulence laden with microparticles, Phys. Fluids 11 (3) (1999) 602–610.

[55] J. Ferry, E. Balachandar, A fast eulerian method for disperse two-phase flow, Int. Journal of Multiphase Flows 27 (2001) 1199–1226.

[56] O. Druzhinin, On the two-way interaction in two-dimensional particle-laden flows - the accumulation of particles a nd flow modification, J. Fluid Mech. 297 (1995) 49–76.

[57] S. Rani, E. Balachandar, Evaluation of the equilibrium eulerian approach for the evolution of particle concentration in isotropic turbulence, Int. Journal of Multiphase Flows 29 (2003) 1793–1816.

[58] S. Rani, E. Balachandar, Preferential concentration of particles in isotropic turbulence: a comparison of the lagrangian and the equilibrium eulerian approaches, Int. Journal of Multiphase Flows 141 (1-2) (2004) 109–118.

[59] S. Chapman, T. Cowling, The Mathematical Theory of Non-Uniform Gases, cambridge mathematical library Edition, Cambridge University Press, 1939.

[60] O. Simonin, Gas particules, Cours d'options, École Nationale Superieure d'Electrotechnique, d'Electronique, d'Informatique, d'Hydraulique et des Télécommunications. (2002).

[61] P. Février, O. Simonin, Statistical and continuum modelling of turbulent reactive particulate flows. part 2: Application of a two-phase second-moment transport model for prediction of turbulent gas-particle flows, in: Theoretical and Experimental Modeling of Particulate Flows, Lecture Series 2000-06, von Karman Institute for Fluid Dynamics, Rhode Saint Genese (Belgium), 2000.

[62] M. Moreau, B. Bédat, O. Simonin, A priori testing of subgrid stress models for Euler-Euler two-phase LES from Euler-Lagrange simulations of gas-particle turbulent flow, in: 18th Ann. Conf. on Liquid Atomization and Spray Systems, ILASS Americas, 2005.

[63] A. Favre, Statistical equations of turbulent gases, in: Problems of hydrodynamics and continuum mechanics, SIAM, Philadelphia, 1969, pp. 231–266.

[64] O. Simonin, P. Février, J. Laviéville, On the spatial distribution of heavy-particle velocities in turbulent flow: from continuous field to particulate chaos, J. of Turb. 3, 040 (2002).

[65] E. Riber, M. Moreau, O. Simonin, B. Cuenot, Towards large eddy simulation of non-homogeneous particle laden turbulent gas flows using Euler-Euler approach, in: 11^{th} Workshop on Two-Phase Flow Predictions, Merseburg, Germany, 2005.

[66] P. Moin, K. Squires, W. Cabot, S. Lee, A dynamic subgrid-scale model for compressible turbulence and scalar transport, Phys. Fluids A 3 (11) (1991) 2746–2757.

[67] B. Vreman, B. Geurts, H. Kuerten, Subgrid modeling in LES of compressible flow, Appl. Sci. Res. 54 (1995) 191–203.

[68] A. Yoshizawa, Statistical theory for compressible turbulent shear flows, with the application to subgrid modeling, Phys. Fluids 29 (7) (1986) 2152–2164.

[69] E. Riber, M. García., V. Moureau, H. Pitsch, O. Simonin, T. Poinsot, Evaluation of numerical strategies for LES of two-phase reacting flows, in: Proc. of the Summer Program, Center for Turbulence Research, NASA Ames/Stanford Univ., 2006, pp. 197–211.

[70] A. Kaufmann, M. Moreau, O. Simonin, J. Hélie, Comparison between lagrangian and mesoscopic eulerian modelling approaches for inertial particles suspended in decaying isotropic turbulence, J. Comput. Phys. 227 (13) (2008) 6448–6472.

[71] K. Hishida, K. Takemoto, M. Maeda., Turbulent characteristics of gas-solids two-phase confined jet, Japanese Journal of Multiphase Flow 1 (1) (1987) 56–69.

[72] T. Poinsot, S. Lele, Boundary conditions for direct simulation of compressible viscous flows, J. Comput. Phys. 101 (1992) 104–129.

[73] I. Celik, A. Smirnov, J. Smith, Appropriate initial and boundary conditions for LES of a ship wake, in: Proc. of the 3^{rd} ASME/JSME Joint Fluids Engineering Conference, Vol. FEDSM99-7851, San Francisco, California, USA, 1999.

[74] A. Smirnov, S. Shi, I. Celik, Random flow generation technique for large eddy simulations and particle-dynamics modeling, Trans. ASME. Journal of Fluids Engineering 123 (2001) 359–371.

[75] A. Sengissen, T. Poinsot, J. VanKampen, J. Kok, Response of a swirled non-premixed burner to fuel flow rate modulation, Lecture Notes in Computational Science and Engineering - Complex effects in LES 56 (2006) 337–351.

[76] B. Vreman, Direct and large eddy simulation of the compressible turbulent mixing layer, Phd thesis, University of Twente (1995).

[77] J. Jiménez, P. Moin, The minimal flow unit in near-wall turbulence, J. Fluid Mech. 225 (1991) 213–240.

[78] Y. Dubief, F. Delcayre, On coherent-vortex identification in turbulence, J. of Turb. 1 (2000) 1–22.

[79] J. Hunt, A. Wray, P. Moin, Eddies, stream, and convergence zones in turbulent flows, in: Proc. of the Summer Program, Center for Turbulence Research, NASA Ames/Stanford Univ., 1988, pp. 193–208.

[80] F. Hussain, J. Jeong, On the identification of a vortex, J. Fluid Mech. 285 (1995) 69–94.

[81] R. D. Williams, Performance of dynamic load balancing algorithms for unstructured mesh calculations, Concurrency: Practice, and Experience 3 (5) (1991) 451–481.

List of Figures

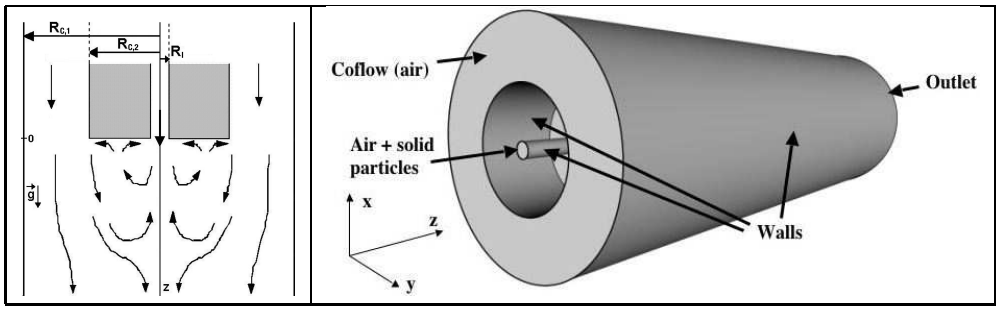

Figure 1. Configuration of Borée *et al.* [1]. The dimensions are: $R_I = 0.010\ m$, $R_{C,1} = 0.075\ m$, $R_{C,2} = 0.150\ m$. The ducts and the chamber are respectively $2\ m$ and $1.5\ m$ long.

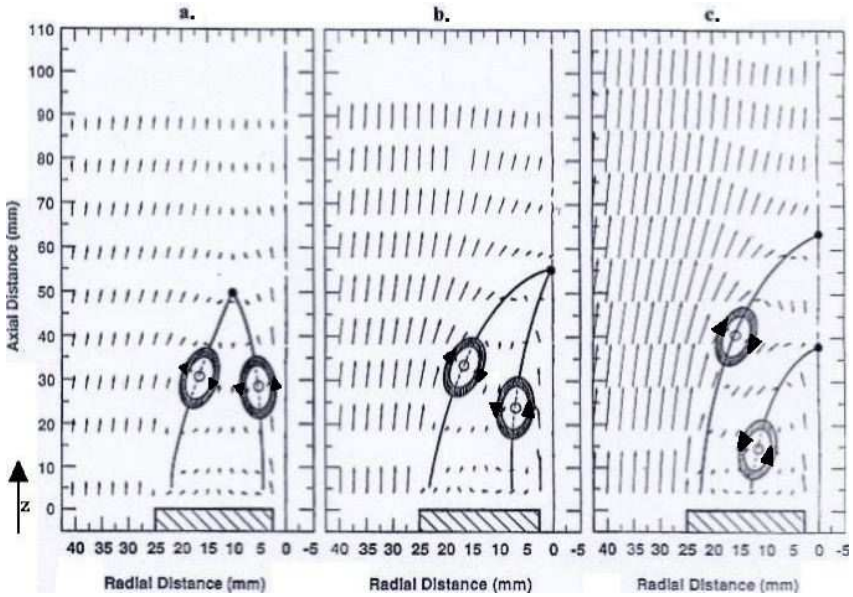

Figure 2. Plots of the measured mean velocity vectors in a bluff body stabilized methane jet for $\bar{U}_{f,I}/\bar{U}_{f,C} = 2.8$ (a.), $\bar{U}_{f,I}/\bar{U}_{f,C} = 1.4$ (b.), and $\bar{U}_{f,I}/\bar{U}_{f,C} = 0.84$ (c.). Black dots show the location of the stagnation points and round arrays give the direction of rotation of the shear layer vortices. From Schefer *et al.* [17].

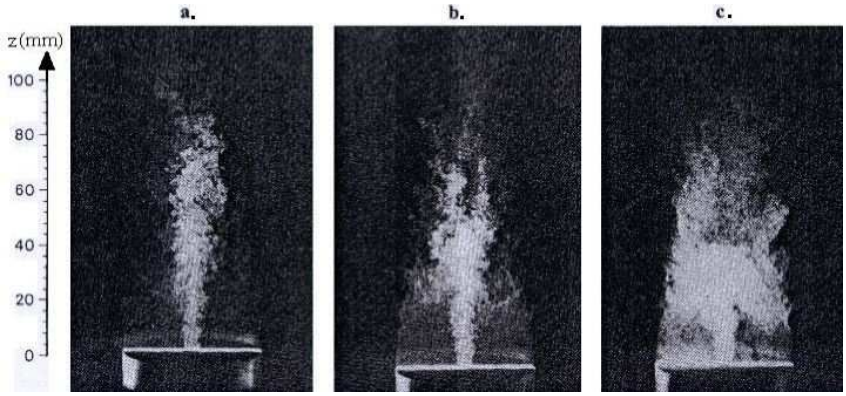

Figure 3. Mie scattering measurements of the instantaneous particle distribution in a bluff body stabilized methane jet for $\bar{U}_{f,I}/\bar{U}_{f,C} = 2.8$ (a.), $\bar{U}_{f,I}/\bar{U}_{f,C} = 1.4$ (b.), and $\bar{U}_{f,I}/\bar{U}_{f,C} = 0.84$ (c.). From Schefer *et al.* [17].

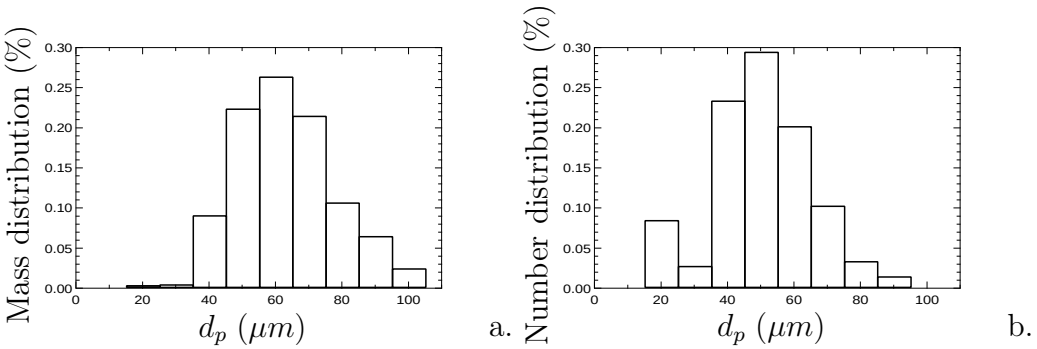

Figure 4. Experimental initial mass (a.), and number (b.) distribution of the particle size.

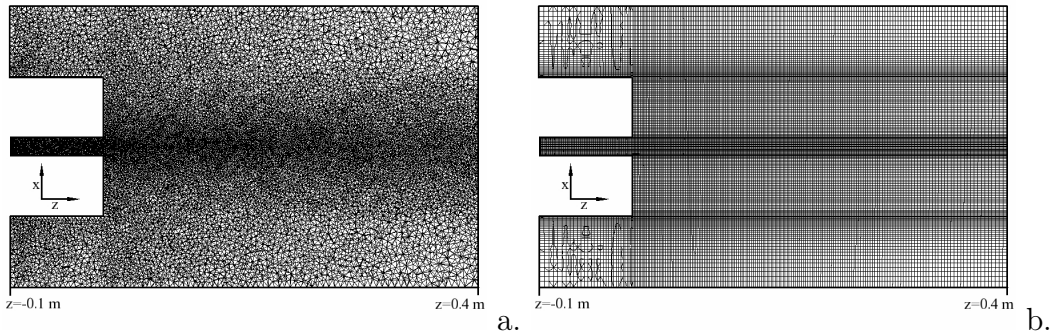

Figure 5. Longitudinal cutting plane ($y = 0$) of the two grids tested: *gridtet* (a.) and *gridhex* (b.) - detail of the region $z \in [-0.1; 0.4]$ m

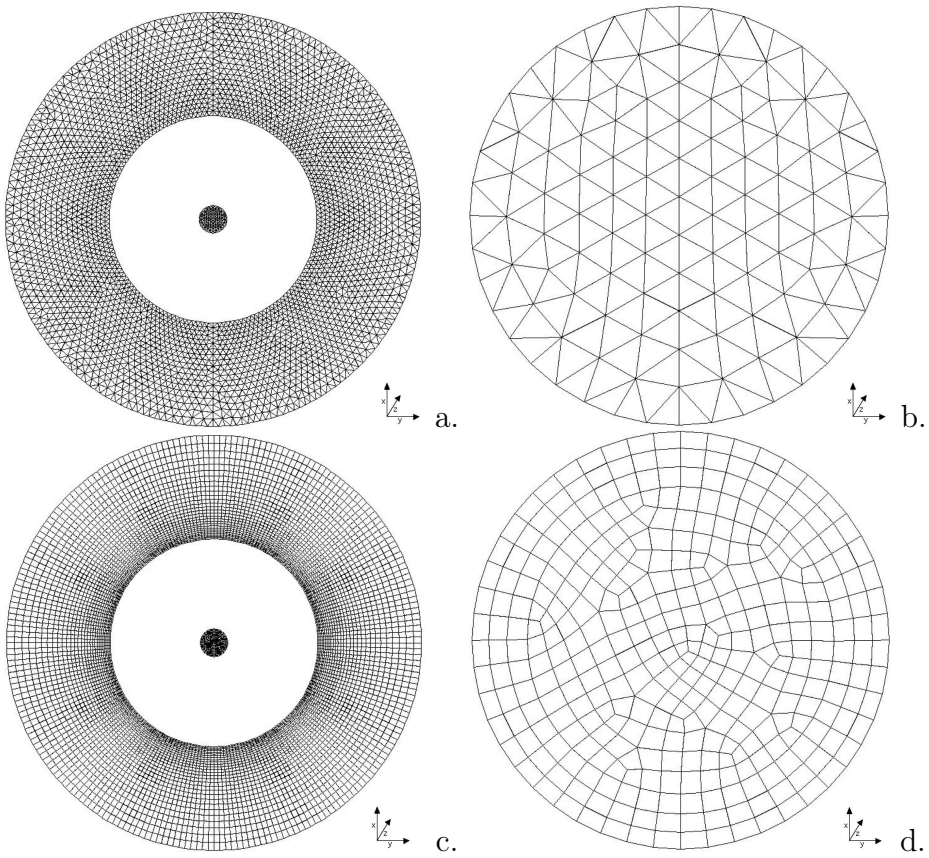

Figure 6. Global front view (left) and detail of the inner inlet (right) for the two grids tested: *gridtet* (a. and b.) and *gridhex* (c. and d.).

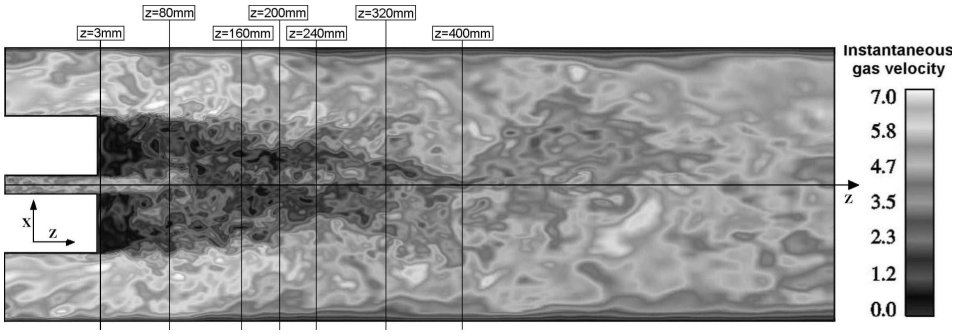

Figure 7. Instantaneous field of velocity modulus obtained with case *avbp_hex_ttgc_rfg* in the cutting plane $y = 0$. The seven vertical lines represent the experimental stations.

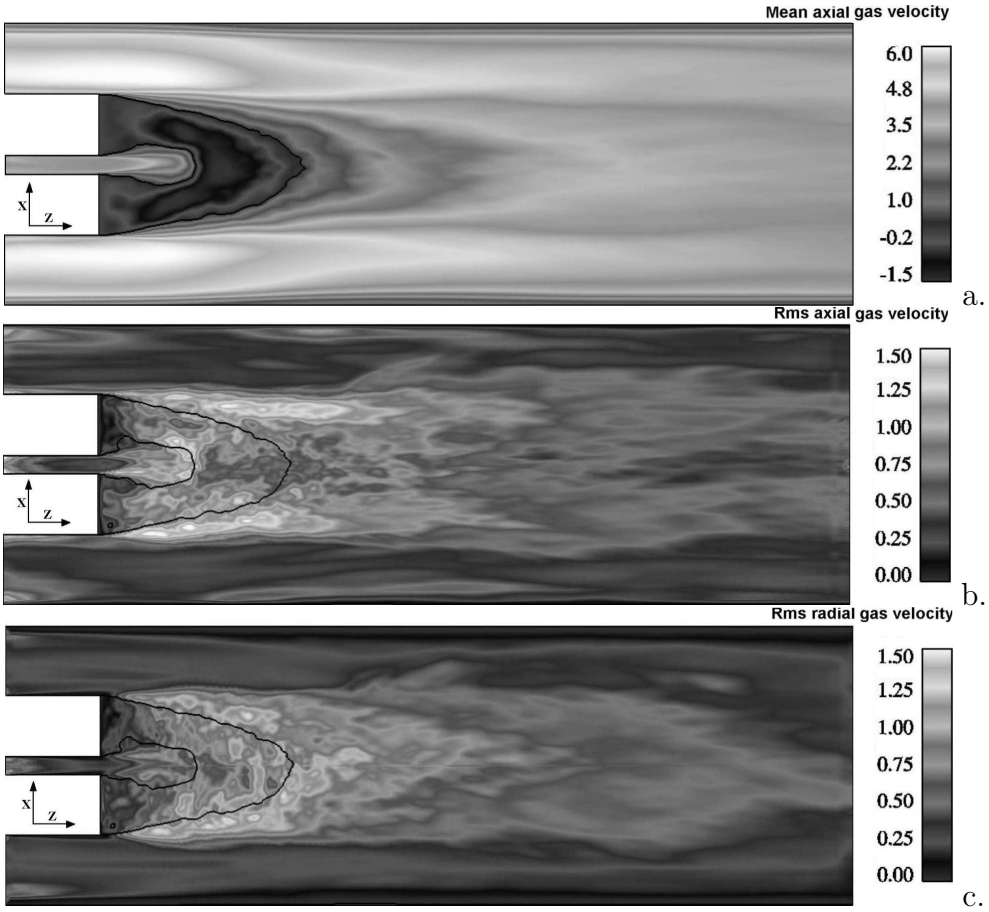

Figure 8. Mean fields of gas axial velocity (a.), and RMS fields of gas axial (b.) and radial (c.) velocity obtained with case *avbp_hex_ttgc_rfg* in the cutting plane $y = 0$. The black line corresponds to the iso-contour line $\langle W_f \rangle = 0$.

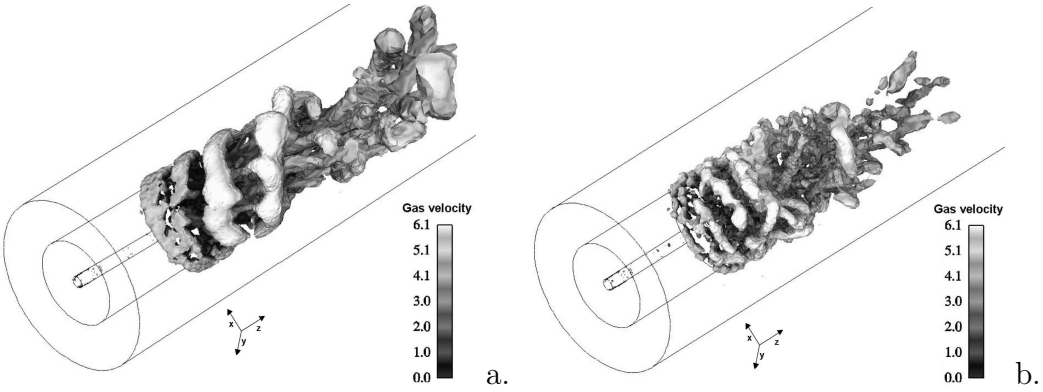

Figure 9. Instantaneous iso-surfaces of Q-criterion for LW (a.), and TTGC (b.). The iso-surfaces are colored by instantaneous velocity. (Simulations performed with AVBP).

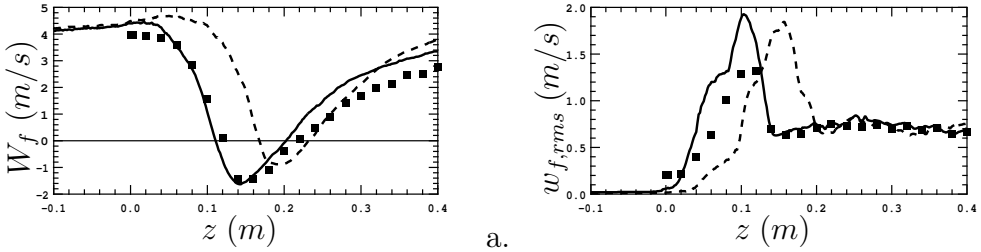

a. b.

Figure 10. Axial profiles of mean (a.), and RMS (b.), axial gas velocity. Symbols: experiment – Dashed line: LW – Solid line: TTGC. (Simulations performed with AVBP).

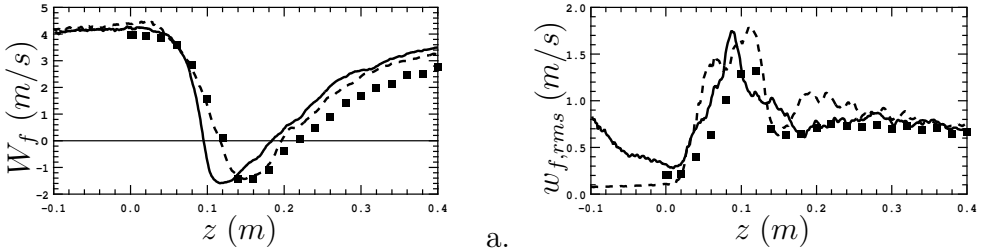

a. b.

Figure 11. Axial profiles of mean (a.), and RMS (b.), axial gas velocity. Symbols: experiment – Dashed line: no injected turbulent fluctuations – Solid line: turbulent fluctuations injected at inlet. (Simulations performed with AVBP).

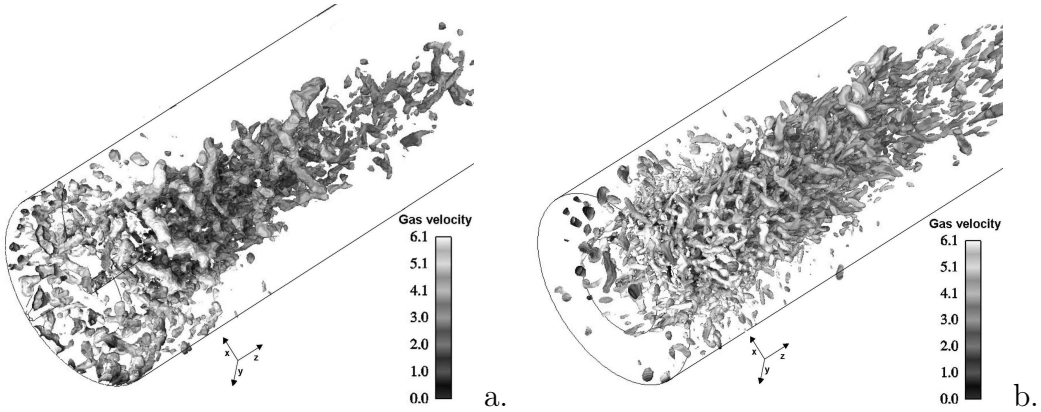

Figure 12. Instantaneous iso-surfaces of Q-criterion for *gridtet* (a.), and *gridhex* (b.). The iso-surfaces are colored by instantaneous velocity. (Simulations performed with AVBP).

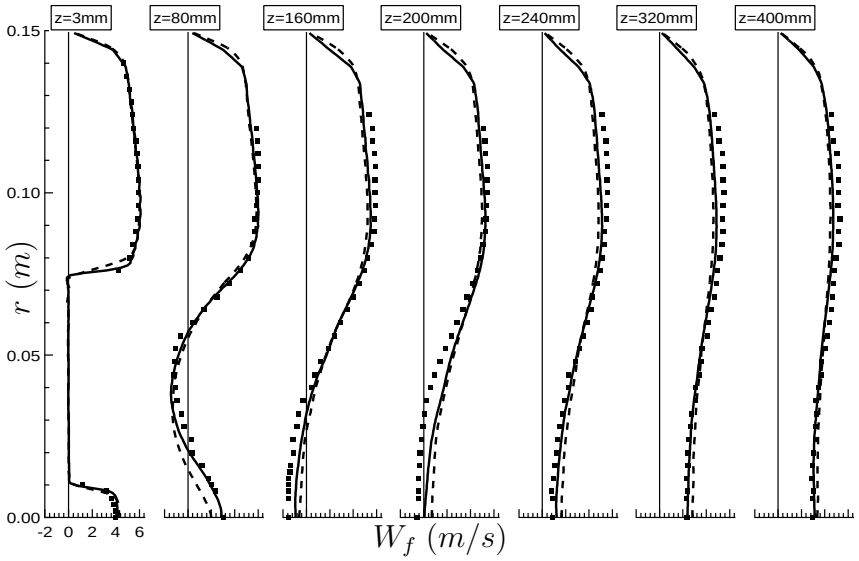

a.

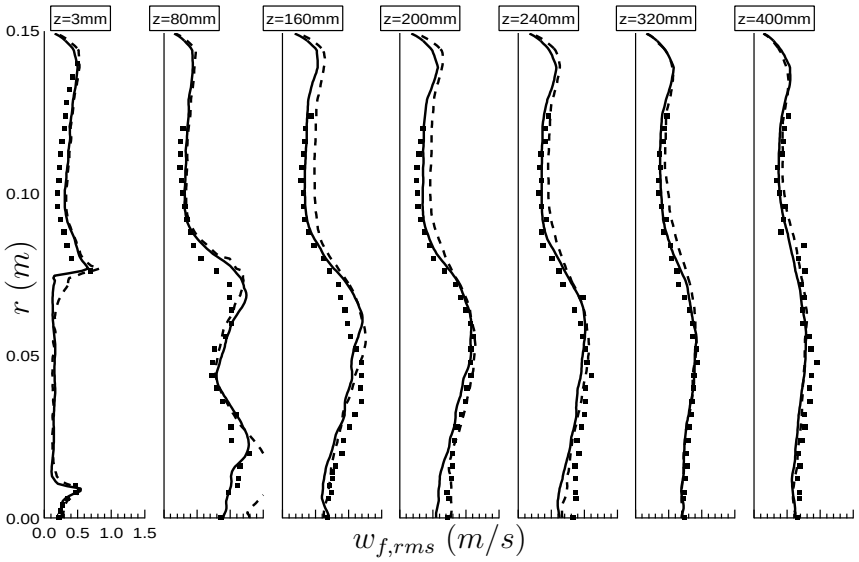

b.

Figure 13. Radial profiles of mean (a.), and RMS (b.), axial gas velocity. Symbols: experiment – Dashed line: *gridtet* – Solid line: *gridhex*. (Simulations performed with AVBP).

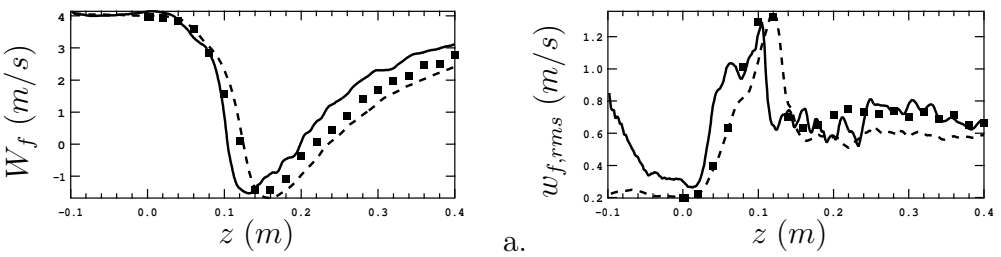

Figure 14. Axial profiles of mean (a.), and RMS (b.), axial gas velocity. Symbols: experiment – Solid line: AVBP – Dashed line: CDP.

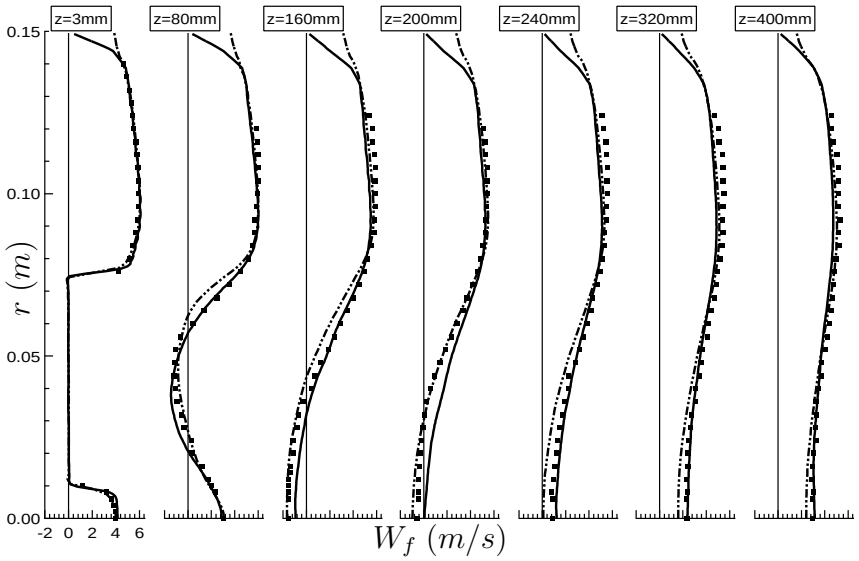

a.

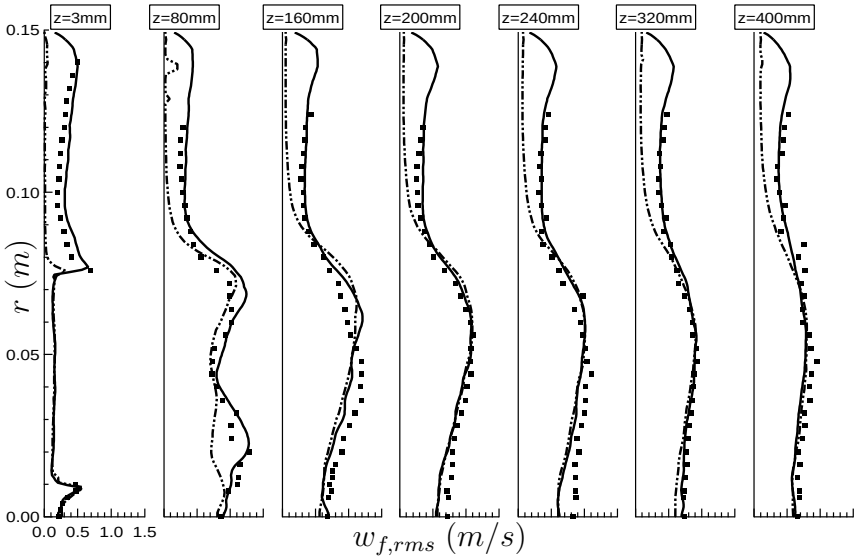

b.

Figure 15. Radial profiles of mean (a.), and RMS (b.), axial gas velocity. Symbols: experiment – Solid line: AVBP – Dot-dashed line: CDP.

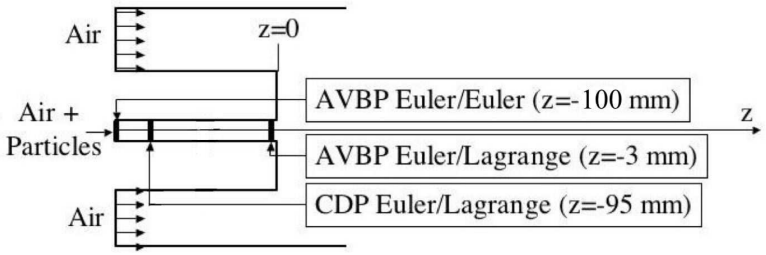

Figure 16. Location of the particle injection depending on the two-phase flow solver used.

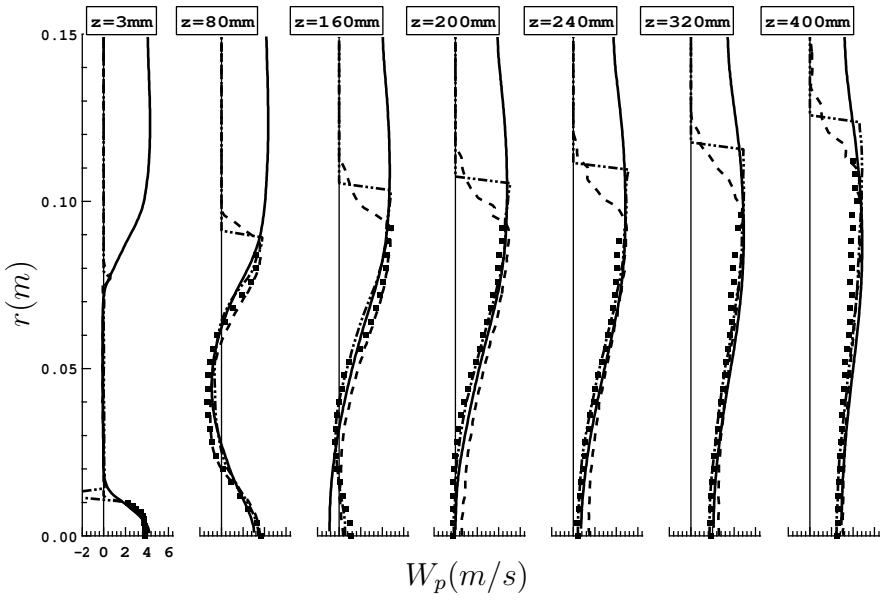

a.

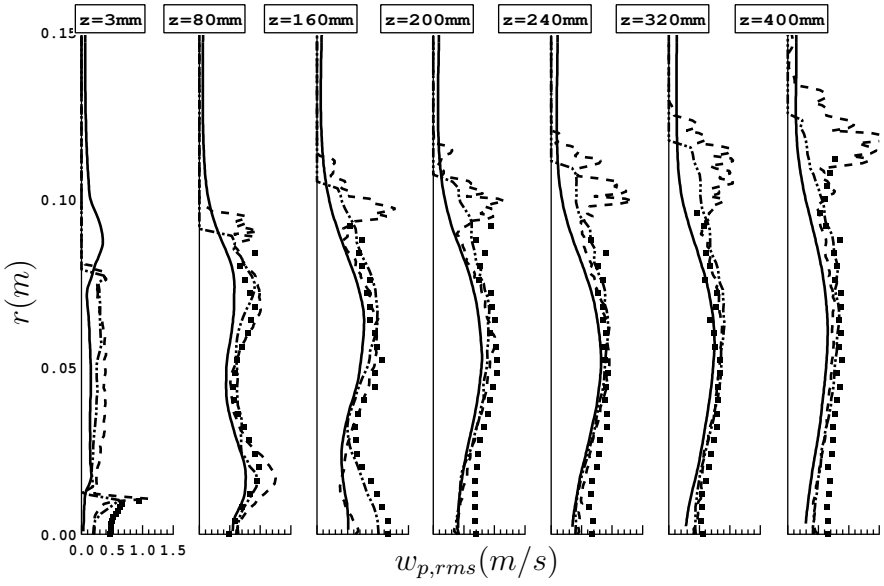

b.

Figure 17. Radial profiles of mean (a.) and RMS (b.) axial particle velocity. Symbols: experiment – Solid line: AVBP-EE – Dashed line: AVBP-EL – Dot-dashed line: CDP-EL.

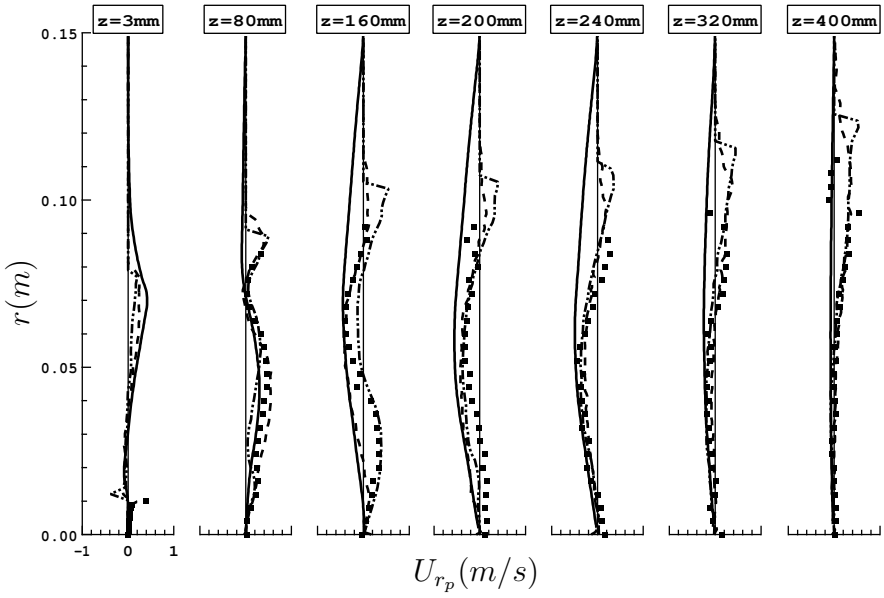

a.

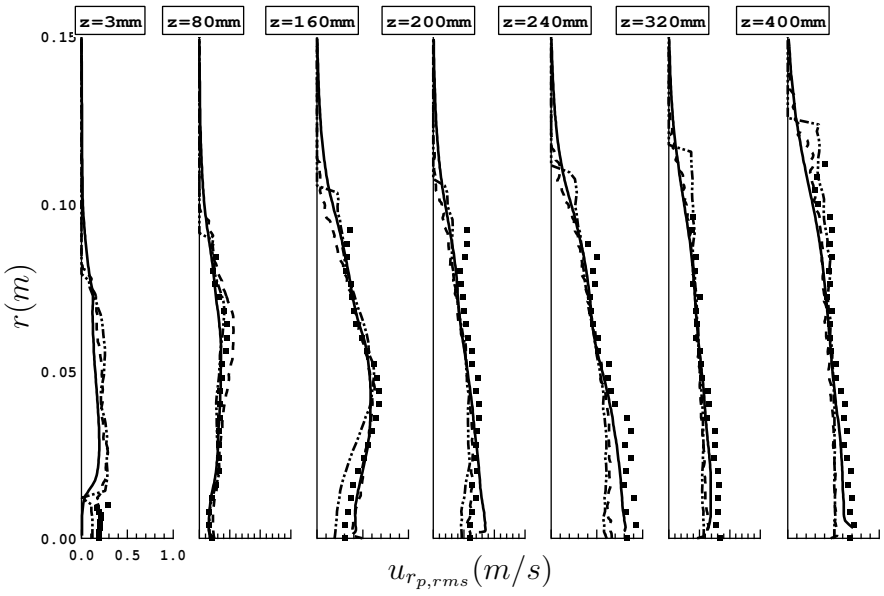

b.

Figure 18. Radial profiles of mean (a.) and RMS (b.) radial particle velocity. Symbols: experiment – Solid line: AVBP-EE – Dashed line: AVBP-EL – Dot-dashed line: CDP-EL.

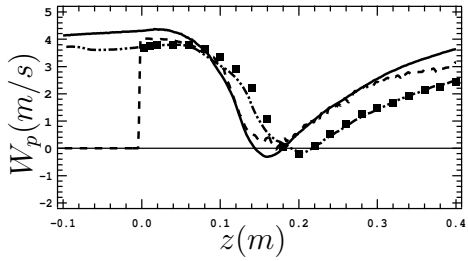

a.

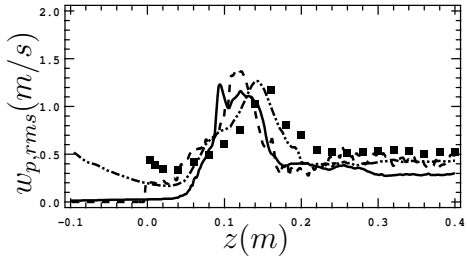

b.

Figure 19. Axial profiles of mean (a.) and RMS (b.) axial particle velocity. Symbols: experiment – Solid line: AVBP-EE – Dashed line: AVBP-EL – Dot-dashed line: CDP-EL.

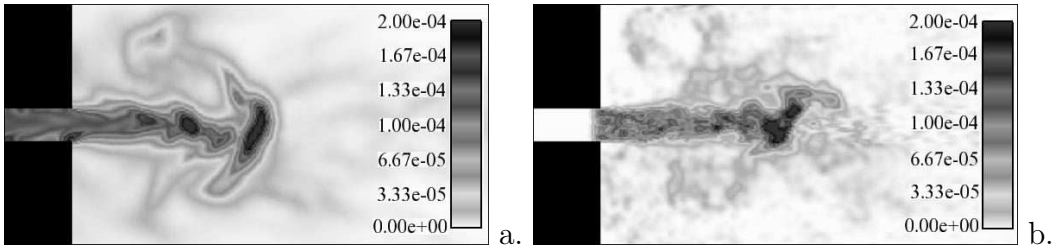

Figure 20. Instantaneous particle volume fraction field in the central plane obtained with the cases *avbp_EE_hex* (a.) and *avbp_EL_hex* (b.).

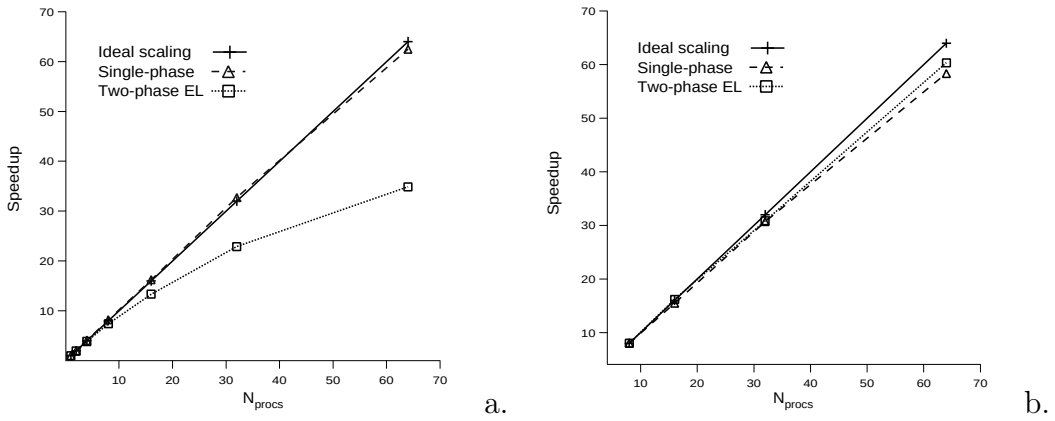

Figure 21. Speedup of the single-phase and the monodisperse test case with *gridtet* (a.) and *gridhex* (b.) on a CRAY XD1 supercomputer. (Simulations performed with AVBP-EL).

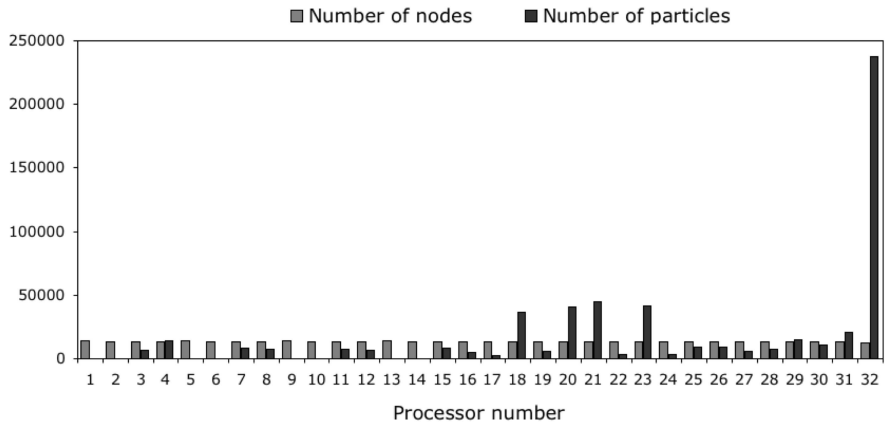

a.

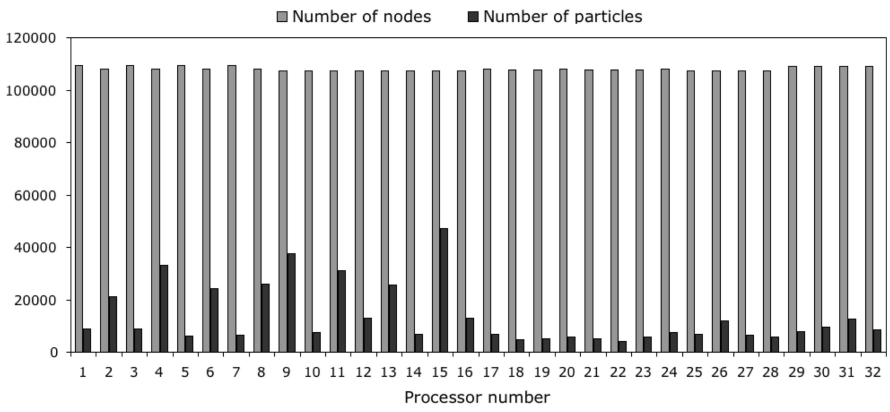

b.

Figure 22. Number of nodes and particles per processor for a 32-partition by using a recursive inertial bisection (RIB) partitioning algorithm for *gridtet* (a.) and *gridhex* (b.). (Simulations performed with AVBP-EL).

List of Tables

Gas phase	**Inner pipe**	**Annular pipe**
Radius (m)	0.010	0.075
Volume flux $(m^3.h^{-1})$	3.4	780
Mean velocity $(m.s^{-1})$	3.4	4.1
Max velocity $(m.s^{-1})$	4.	6.
Reynolds number $(-)$	4500	40,000

Table 1
Characteristics of the gas phase at the outlet of the inner and annular pipes.

$\mathbf{d_p}$ (μm)	20	30	40	50	60	70	80	90	100
$\tau_\mathbf{p}$ (ms)	3.1	6.9	12.3	19.2	27.6	37.6	49.1	62.2	76.7
$\mathbf{St}$ $(-)$	0.4	1.0	1.8	2.7	3.9	5.4	7.0	8.9	11.0

Table 2
Experimental particle relaxation time and Stokes number depending on particle diameter.

Name	**gridtet**	**gridhex**
Grid type	Tetrahedra	Hexahedra
Number of nodes	549,369	3,255,085
Number of cells	3,115,898	3,207,960
Length of the pipes (m)	0.1	0.1
Length of the chamber (m)	1.5	0.8
Total volume of the domain (m^3)	0.111	0.062
$\mathbf{y^+}$ **in the inner pipe** (-)	15	7.5
$\mathbf{y^+}$ **in the coflow** (-)	64	15

Table 3
Characteristics of the two grids tested.

Case	Solver	Grid	Scheme	Inlet treatment
avbp_tet_lw_norfg	AVBP	gridtet	LW	none
avbp_tet_ttgc_norfg	AVBP	gridtet	TTGC	none
avbp_tet_ttgc_rfg	AVBP	gridtet	TTGC	RFG
avbp_hex_ttgc_rfg	AVBP	gridhex	TTGC	RFG

Table 4
Test cases computed with AVBP and corresponding parameters.

Case	Total CPU time (μs)	Efficiency / iteration / node (μs)	Efficiency / iteration / cell (μs)
avbp_tet_lw_norfg	28,527	1.81	0.32
avbp_tet_ttgc_rfg	68,460	4.35	0.77
avbp_hex_ttgc_rfg	235,823	3.06	3.10

Table 5
Code efficiency for single-phase flow calculations depending on the scheme and the grid. Statistics given for 0.1 s (physical time) computed with TTGC on 16 processors on a CRAY XD1 supercomputer.

Case	avbp_hex_ttgc_rfg	cdp_hex
Solver	AVBP	CDP
Time step (μs) / **CFL**	4.22 / 0.7	147 / 50
Averaging time (s) / **iterations**	1. / 192,000	2.65 / 18,000
Convective scheme	TTGC (3^{rd} order) [4]	2^{nd} order kinetic energy conserving [36]
SGS model / Wall model	WALE / None	Dynamic Smagorinsky / None
Inner jet / Coflow Inlet BC	Forcing / Forcing	Forcing / No forcing

Table 6
Comparison of the parameters and models used for the single-phase flow LES performed with AVBP and CDP on the hexahedron-based grid *gridhex*.

	cdp_EL_hex	**avbp_EL_hex**	**avbp_EE_hex**
Averaging time (s)	4.0	0.5	1.0
Grid	gridhex	gridhex	gridhex
Particle mean axial velocity	Experimental profile	Experimental profile	Experimental profile
Turbulent fluctuations	White noise (10 %)	White noise (12 %)	Zero
Particle distribution	Homogeneous	Homogeneous	Experimental profile

Table 7
Summary of two-phase flow test cases and parameters used for the particle injection.

N_{procs}	1	2	4	8	16	32	64
Single-phase	1	0.50	0.25	0.12	0.06	0.030	0.016
Two-phase EL	1.05	0.54	0.27	0.14	0.08	0.046	0.030

Table 8
Summary of the CPU time ratios of AVBP-EL with *gridtet* on a CRAY XD1 supercomputer.

N_{procs}	8	16	32	64
Single-phase	1	0.51	0.26	0.137
Two-phase EL	1.06	0.524	0.275	0.14

Table 9
Summary of the CPU time ratios of AVBP-EL with *gridhex* on a CRAY XD1 supercomputer.